MAGNETIZATION AND TRANSPORT STUDY OF DISORDERED WEAK ITINERANT FERROMAGNETS

A dissertation submitted
To Kent State University in partial
Fulfillment of the requirements for the
Degree of Doctor of Philosophy

By

Sara Ubaid Kassis

August, 2009

Dissertation written by
Sara Ubaid Kassis
B.S., Cleveland State University, 2001
Ph.D., Kent State University, 2009

Approved by

_____Almut Schroeder _____, Chair, Doctoral Dissertation Committee

_____Carmen Almasan_____, Members, Doctoral Dissertation Committee

_____David Allender_____

_____Songping Huang_____

_____Robert Twieg_____

Accepted by

_____Bryon Anderson_____, Chair, Department of Physics

_____Timothy Moerland_____, Dean, College of Arts and Sciences

ii

Table of Contents

`

List of Figures

vii

List of Tables

Acknowledgements

First, I wanted to thank my advisor and mentor, Dr. Almut Schroeder, for her continuous support and encouragement during my years as her graduate student. I am grateful to her for being patient and understanding. I appreciate that she always made time for stimulating discussions, even when it took up most of her day. It has been a great pleasure working under her guidance. I want to thank Dr. Carmen Almasan, whose generosity made it possible to utilize the SQUID magnetometer in her lab, which without I would not have been able to obtain most of the results for my dissertation. I wanted to also thank her for lending us her tube furnace which was used to anneal our samples. I wanted to thank Dr. Song-Ping Huang for the generous use of his X-Ray Diffractometer which I used to find the crystal structure of my samples. Thanks to Dr. Thomas Vojta for the stimulating discussions. Many thanks go to my fellow graduate student and friend, Bilal El Zoghbi who painstakingly spent endless hours making the ac pickup coil for our lab. Thanks for all his help around the lab and for all the discussions and laughs. Thanks to undergraduates Ben Rohr, and Brendan Wyatt who worked over the summer months and prepared some of my samples. Thanks to Dr. Hong Xiao, Tao Hu, Dr. Tika Katuwal, and Parshu Gyawali for all of their help with the SQUID, and especially with the helium fills. Thanks to Larry Maurer who is one of the most meticulous glass blowers I have ever met, who sealed all of our quartz tubes for annealing. Thanks for all the enlightening conversations and laughs. Thanks to Wade Aldhizer for all his help with machining parts

Chapter 1

General Introduction and Basic Concepts

Magnetism of materials is an old phenomenon whose origin was understood about a century ago. The first microscopic models of magnets were developed using the notion that magnetic order can arise from interactions between magnetic moments of the electrons confined to the atom (1). Shortly after, Stoner proposed the first model for itinerant electrons, where magnetic order can arise due to interacting conduction electrons carrying a spin rather than from the local moments. These interacting itinerant electron systems, or strongly correlated electron systems, remain a challenge in condensed matter physics today for theorists and experimentalists and can lead to remarkable physical properties. In particular, alloys that contain transition metal ions with a partially filled d-electron shell, or rare earth metal ions with f electrons, can exhibit magnetic ordered phases or just paramagnetism (PM), but also more exotic states like unconventional superconductivity and non-Fermi liquid behavior, not expected in a normal metal. One route to understand unconventional phases is the systematic study of a quantum phase transition (QPT) [see e.g. in references (2), (3), (4), (5), (6), (7)] which is a change of the ground state at 0 K at a quantum critical point (QCP), e.g. from a magnetic ordered to a nonmagnetic ordered state.

Two decades ago, it was observed that $U_xY_{1-x}Pd_3$ was the first compound to show unusual exponents in the temperature dependence of the specific heat, C, magnetic susceptibility, χ, and the electrical resistivity, ρ (8) (9) which are not expected for a normal metal. Typically, the fundamental concept for a normal metal can be described as a Fermi liquid (FL), which considers the conduction electrons as a weakly interacting gas of Fermi particles called quasiparticles with a finite lifetime around the Fermi energy. However, when the interactions between the electrons are strong and long-ranged, which can occur in strongly correlated electron systems, the lifetime of the quasiparticles is diminished. This fundamental concept of a metal, the Fermi liquid description, breaks down, where the quasiparticles and the Fermi energy are not well defined anymore and a new description is needed. Typical signatures of this so-called non-Fermi liquid (NFL) behavior are power laws in the temperature dependencies of the specific heat, magnetic susceptibility, and the resistivity. Other strongly correlated electron materials have been found to show NFL behavior (6), and the search continues to understand the origin of the breakdown of this fundamental concept for metals. Strongly correlated compounds include high T_c superconductors which show NFL in the normal conducting phase, transition metal alloys, and Heavy Fermion compounds (HF) which are f-electron alloys. In particular, NFL behavior has been observed close to a quantum critical point, e.g. near the onset of magnetic ordering, and can be achieved when the order is tuned through an external driving mechanism such as external pressure, chemical substitution (alloying), or magnetic field [see e.g. (6)].

The most experimental evidence of NFL have been typically seen in Heavy Fermion systems close to an antiferromagnetic quantum critical point, when the magnetic state of the alloy is driven from an antiferromagnetic ordered phase into a paramagnetic phase through external pressure or chemical substitution [see e.g. (6)]. For instance, $CePd_2Si_2$ is a HF compound that shows antiferromagnetic order below 10 K (10), but when sufficient pressure is applied the ordering temperature is reduced to zero. In the vicinity of this quantum critical point, the resistivity shows unusual power laws, indicating NFL behavior, and also the onset of a superconducting phase. A specific power in the resistivity could be due to critical antiferromagnetic fluctuations caused by the strong interactions between the conduction electrons, which also offer a coupling mechanism for unconventional superconductivity. In contrast, Heavy Fermion systems close to a ferromagnetic quantum critical point are not as common. In fact, there are only a few examples of ferromagnetic HF discovered which show NFL behavior close to a FM phase transition such as $URu_{2-x}Re_xSi_2$ (11) and $Th_{1-x}U_xCu_2Si_2$ (12). Beside NFL behavior, the onset of a superconducting phase was discovered in UGe_2 (6) where the ferromagnetic order is suppressed with the application of pressure.

Alternatively, ferromagnetic (FM) order with a low critical temperature has been extensively studied in d transition metal alloys [see e.g. (13), (14), (15), (16)]. Some well known examples are $ZrZn_2$ and MnSi. The well-studied, $ZrZn_2$, is considered a model system for weak itinerant ferromagnets. The critical temperature is very small and it shows signs of NFL close to a pressure driven ferromagnetic quantum critical point. MnSi is an itinerant ferromagnet with a low transition temperature which can be reduced

to a zero with the application of pressure [see e.g. (17) and ref. therein] and shows NFL behavior, but it also shows a new unconventional phase of partial order reminiscent of liquid crystals (18). Even the ferromagnetic state in iron can be suppressed and show superconductivity at very high pressure (19).

Various ferromagnetic quantum critical points displaying signs of NFL behavior are pressure induced, but many itinerant ferromagnetic materials can be tuned by chemical substitution. On one hand, a small amount of doping in the itinerant binary alloy Ni_xPd_{1-x} induces ferromagnetic ordering at the critical concentration of $x_c \approx 0.026$ (20) and shows NFL behavior in the resistivity, specific heat, and the susceptibility (21) which is consistent with the predictions with a clean FM QCP (22). On the other hand, the compound Ni-Cu (23) does not show simple power laws in the resistivity around the critical concentration of 44% nickel when ferromagnetic order disappears. This complicated behavior is attributed to the existence of giant moment clusters which are induced by chemical substitution. Chemical substitution does not only change the interaction between electrons, it also might introduce inhomogeneities which change the scenario of the quantum phase transition. Although there are many examples, it is not clear how much disorder is present and how it affects the NFL behavior in transition metal alloys. Some questions arise that need to be addressed: How can one introduce disorder to a system and systematically control it? Will a QCP remain the same in this scenario or will it be modified? Is the NFL behavior different in an inhomogeneous system? Will any new exotic behavior be seen? New theories have recently been

developed to include the effect of disorder on a QCP, leading the system to form a new QCP (24) different than in a clean system.

In this dissertation, I chose to study the weak itinerant ferromagnetic binary alloy system of ferromagnetic nickel diluted with non magnetic vanadium. It has been previously studied (25), (26) and is known for its tunable ferromagnetic critical temperature, T_c, essentially used in magnetic recording tapes (27). The critical temperature rapidly decreases upon dilution with only a small amount of vanadium. In this regime, NFL behavior has been observed in the resistivity (28) over a range of concentrations. Additionally, it has also been reported that the disorder induces large magnetic clusters, also observed in Ni-Cu (29) and Pd-Ni (30). The odd power law in the resistivity and the magnetic clustering make Ni-V an ideal candidate to probe for the predictions for disordered QCP, such as a Griffiths phase.

The first chapter is an overview for weak itinerant ferromagnets, including a description of non-Fermi liquid behavior and quantum phase transitions. Chapter two explains the experimental methods used in obtaining the data. Chapter three provides the main focus of this dissertation presenting detailed experimental results for the Ni-V compound and a discussion on how it is compared to recent theories addressing a disordered quantum phase transition, QPT. In order to comprehend the experimental results found from Chapter 3, it is essential to understand the physics of itinerant magnets, of QPT, and non Fermi liquid behavior and the interplay that leads to novel phases in this complex material.

.

1.1 Localized and Itinerant Magnetism

Magnetism in metals can be considered to arise from the interaction of two different extremes of electron wavefunctions: localized and itinerant (which are delocalized moments). Electrons that are bound to the parent atom might have a magnetic moment due to incomplete shells which are due to orbital and spin contributions, whereas the itinerant electrons are not bound to a single atom and the magnetic moment here predominantly comes from the spin ½. Additionally, the 3d and the 4s electrons are both itinerant in the transition metals contributing to transport properties, but the magnetic moment is mostly due to the 3d electrons. Localized and itinerant electrons show a different magnetic response, even for non-interacting electrons. But before this is elaborated on, a simple description of magnetization is needed.

An electron is a negative charge with a spin and in a simple model is thought to orbit around the parent atom. Magnetization can come from the magnetic dipole moment of the spins or from the orbital angular momentum, although the former mostly contributes. The equation for the magnetic moment, μ, is given by [see e.g. (31); (32)]

$$\mu = -g\mu_B J \tag{1}$$

where the g factor for an electron spin is 2, μ_B is the magnetic moment for one electron and is known as the Bohr magneton, defined to be $\mu_B = e\hbar/2mc = 9.274e^{-24}$ J/T, and J is the total angular momentum. Interactions between electrons occur, but for a basic description of magnetization non-interacting electrons will suffice.

For independent local magnetic moments with spin ½, a magnetic field, H, will cause the spins to align in the direction of the field causing magnetism to arise through a paramagnetic contribution due to the Zeeman effect. The thermodynamical average of the magnetic moment gives rise to the magnetization, M, and is given by the Brillouin function

$$M = N\mu \tanh\left(\frac{\mu H}{kT}\right)$$ (2)

where N is the number of particles contributing to magnetism (e.g. electrons), μ is the magnetic moment, H is the magnetic field, k is Boltzmann's constant. The features of independent local moments are a saturation of the magnetization in high magnetic fields and a Curie law at high temperatures. Since the moments align with a magnetic field, the magnetic response will saturate at high magnetic fields giving a maximum value of the magnetization called the saturation magnetization, M_{sat}.

$$M_{sat} = N\mu$$ (3)

In most paramagnetic materials, the saturation magnetization is seen at high magnetic fields and at low temperatures, if it is seen at all. An approximation in low magnetic fields and high temperature gives the paramagnetic contribution to the magnetization

$$M = \frac{N\mu^2 H}{kT}$$ (4)

The Curie susceptibility, χ, is found at high temperatures and is defined as

$$\chi = \frac{M}{H}\bigg|_{H \to 0} = \frac{N\mu^2}{kT} = \frac{C}{T}$$ (5)

The Curie constant, C, is $C = N\mu^2/k$.

A different response is obtained in the delocalized non-interacting case like in the free electron gas. With itinerant electrons, we consider separate spin-up and spin-down bands which are shifted in energy in the presence of an external magnetic field. A transfer of electrons is made from the spin-down to the spin-up electron states at the Fermi surface, causing an imbalance in the amount of spin-up and spin-down electrons, giving rise to net magnetization. The magnetization in this case does not saturate as long as the energy shift is smaller than the band width and is given as

$$M = \frac{N\mu_B^2}{kT_F} H$$

(6)

.

The magnetic susceptibility is known as the Pauli susceptibility which does not show a T dependence in the limit of $\mu_B H \ll kT_F$ and is given as

$$\chi_{Pauli} = \frac{N\mu_B^2}{kT_F}$$

(7)

where μ_B is the Bohr magneton and kT_F is the Fermi energy, which is usually on the order of 10,000 K for normal metals.

In a ferromagnet, the magnetic moments of localized electrons are statistically parallel to each other with an internal interaction between them called the exchange field. Different models have tried to explain the magnetism resulting from these directly interacting local moments. Weiss (33) was the first to claim that the spontaneous magnetization comes from an internal molecular field. Heisenberg (34) added to that and realized an exchange interaction between electronic spins in a quantum many-body problem can describe ferromagnetism. The 3-d Heisenberg model is based on the interaction between two local spin moments is given by the Hamiltonian

$$\hat{H} = -\sum_{i>j} J_{i,j} S_i S_j - g\mu_B \sum_i H_i^z S_i^z \tag{8}$$

where i and j are the spin sites, and $J_{i,j}$ is the interaction between the spins S_i and S_j, H_i^z is a local field in the z direction acting on local spins, and S_i^z is the spin in the z direction. The Heisenberg model is not solvable in general for 3-d, but a mean field approximation describes the main properties of a ferromagnetic system, such as a phase transition taking place at the ordering temperature, T_c, and the onset of spontaneous magnetization as an order parameter for the ferromagnetic phase. This approximation replaces the exchange field between the neighboring spins with an average of the interaction that is dependent on the magnetization, M, and is given by the Hamiltonian, H_{MF}.

$$H_{MFj} = \sum_{i>j} -J_{ij} S_i = \lambda M \tag{9}$$

The field is replaced with an effective field, H_{eff},

$$H_{eff} = H + \lambda M \tag{10}$$

The relation for the magnetization for a paramagnet in an effective magnetic field is

$$M = \chi \cdot H_{eff} = \chi (H + \lambda M) \tag{11}$$

If we substitute the Curie law, $\chi = C/T$, and solve for M we obtain

$$M = \frac{C}{T - C\lambda} \cdot H \tag{12}$$

yielding the Curie-Weiss law, where $\Theta = C\lambda$

$$\chi = \frac{C}{T - \Theta} \, . \tag{13}$$

The Curie-Weiss temperature is $\Theta \approx T_c$ for ferromagnetic interactions. Close to the phase transition, power laws can be predicted for thermodynamical properties such as the

magnetization, magnetic susceptibility, and specific heat. More specific information will be found in a later section of this chapter.

Besides the direct overlap of neighboring orbitals, indirect exchange interactions arise due to local orbitals or conduction electrons and can lead to magnetic order. In a metal, a local moment can introduce magnetization density variations of the electron gas over a long distance which provides a coupling to another local moment. The sign of the interaction oscillates in distance and can be ferromagnetic or antiferromagnetic. This is called the RKKY interaction which becomes important in f-electron alloys and dilute d-electron alloys. If the interaction between the local moment and the screening electron cloud becomes too strong, the local moment gets fully screened. It starts fluctuating and cannot contribute to a magnetic ordered state. This is the Kondo effect which competes with the RKKY interaction leading to a magnetic state with a low ordering temperature or a non-magnetic state as seen in, e.g., Heavy Fermion compounds.

Although the model of direct exchange interactions works well for local electrons, the Heisenberg model does not allow for the electron to change sites, therefore, it is not a general description for an itinerant electron. For this case and for a narrow d-band, the Hubbard model is often applied for, e.g., high T_c superconductors. In this model, the electrons occupy the atomic orbitals and can "hop" between atoms when they conduct, but local interactions between the electrons are taken into account. The magnetism of itinerant electrons was first addressed by the Stoner model (35) to explain the non-integer value of the spontaneous magnetization of electrons at zero temperature. It used the same

concept of Pauli paramagnetism except that the band shift for spin-up and spin-down is caused by an internal magnetic field resulting from the interaction between the particles (1). If the Stoner criterion $I_S D(E_F) > 1$ is satisfied, where I_S is the Stoner parameter and $D(E_F)$ is the density of states at the Fermi surface, the band splitting leads to an energy gain and the system becomes ferromagnetic. Furthermore, different ranges of magnetic order may occur: non-magnetic, weakly ferromagnetic, and strongly ferromagnetic. Stoner predicts the temperature dependent spontaneous magnetization and susceptibility for a weakly interacting system which arises from the temperature dependence of the Fermi distribution as being

$$M(T) = M_0 \left(1 - \frac{T^2}{T_c^2} \right)^{\frac{1}{2}} \tag{14}$$

$$\chi(T) = \chi_0 \left(\frac{T^2}{T_c^2} - 1 \right)^{-1} \quad \text{for } T \geq T_c \tag{15}$$

The model explains important characteristics of the ferromagnetic metals Fe, Co, and Ni where the spontaneous moment/atom is only a fraction of the expected spin value. Although this model works reasonably well for materials such as $ZrZn_2$ at low temperatures (1) and other weakly itinerant systems, Stoner's theory does not predict the temperature dependence of the magnetization and magnetic susceptibility for most systems. This is because even though the MFT approach is used to describe phase transitions, MFT does not work in the critical region surrounding T_c since the theory does not take into account the magnetic moment fluctuations. A refined theory is needed to allow a correct description of both itinerant and localized magnetization.

A more advanced model in describing itinerant magnetism is Spin Fluctuation theory, which takes into account magnetic moment fluctuations close to the critical point, unlike the Heisenberg model, where the local moment size is conserved. This self-consistent renormalization (SCR) theory of Moriya and Kawabata describes the magnetic properties for a broad range of localized to itinerant electron systems (22). It predicts specific exponents, especially for the critical behavior caused by weakly interacting spin fluctuations.

SCR theory enhances the Stoner model by incorporating exchange-enhanced spin fluctuations to calculate the properties of a magnetic metal at finite temperature, which dominate the magnetic excitations in a weak ferromagnet. The theory states that for the vicinity of the critical point in a clean system the corresponding behavior of the susceptibility of a weak itinerant ferromagnet with spin fluctuations is

$$\frac{1}{\chi} \propto \left(T^{\frac{4}{3}} - T_c^{\frac{4}{3}} \right) \tag{16}$$

A Curie law is obtained for $T \gg T_c$ just like for a non-interacting paramagnet. The magnetization of a weak itinerant ferromagnet for temperatures below the critical temperature with spin fluctuations is found in the vicinity of the critical point

$$M^2(T) \propto T_c^{\frac{4}{3}} - T^{\frac{4}{3}} \tag{17}$$

The magnetization of a system at the bulk level is given by the relation of $M = N\mu/V$, where N is the number of magnetic moments in the sample, and V is the volume of the sample.

So, a characteristic of a weak itinerant magnet is a low critical temperature, but also a small spontaneous moment, μ_s, due to spin fluctuations, even in the ordered state. It has been debated whether itinerant magnets exhibit a Curie-Weiss law for $T \gg T_c$, which is derived for local moments. Nevertheless even if moments are fluctuating, a Curie-Weiss law can still be explained by SCR theory, which allows an estimate of an effective moment size in the disordered regime. For $T < T_c$, the ordered magnetic moment per atom is given by μ_{sat}, also known as the saturation moment. For $T > T_c$ the effective moment per atom in the paramagnetic regime is obtained through the Curie-Weiss law and is called the paramagnetic moment, μ_{pm}. For localized moments, the ratio of μ_{pm}/μ_{sat} will be on the order of 1 and for itinerant moments, $\mu_{pm}/\mu_{sat} \gg 1$ (36) ; (37). The ratio of μ_{pm}/μ_{sat} is usually plotted as a function of the Curie temperature in a Rhodes-Wohlfarth (RW) plot (Figure 1.1) for that system. Here, the RW plot uses the notation of q_c as some effective moment, and the translation of this to the effective moment obtained from the Curie-Weiss law is $q_c(q_c + 2) = \mu^2_{pm}$ (38), and the quantity, q_s, is equal to the saturation moment. The curve of the plot is for itinerant electrons to which many elements and compounds fit onto. The dashed line corresponds to systems with localized electrons, and systems that reside in between these limits have magnetization contributing from both localized and itinerant electrons.
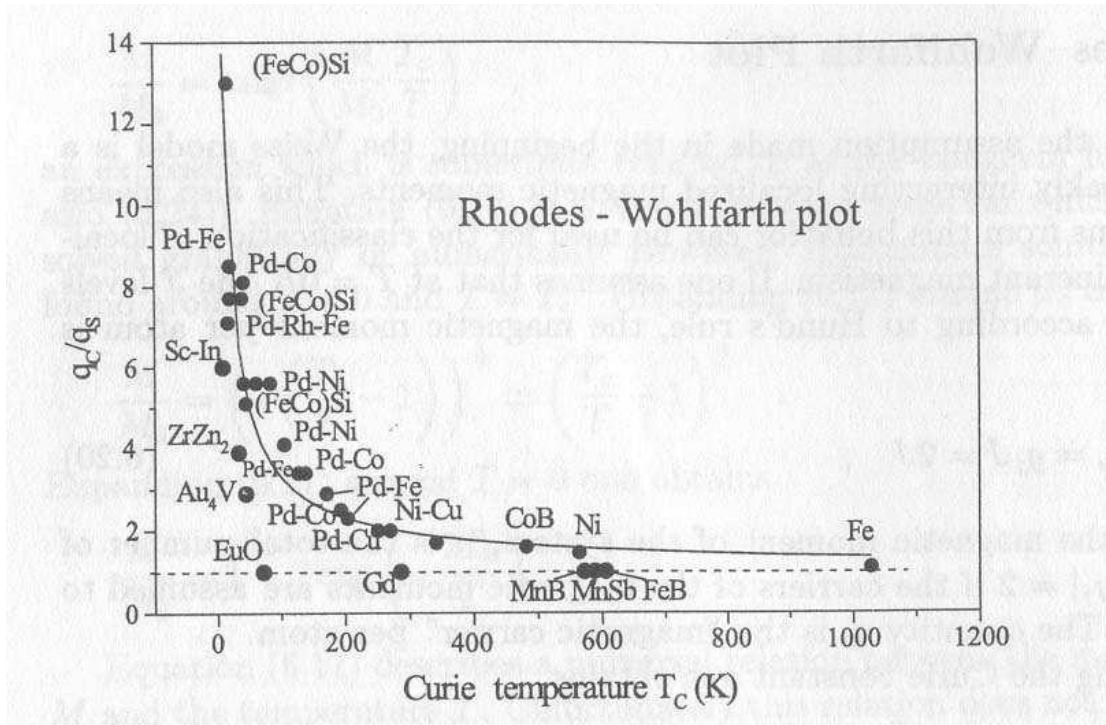
Figure 1.1: Rhodes-Wohlfarth plot showing the ratio of the effective moment over the saturation moment as a function of the critical temperature, T_c. The translation of the RW moment to the effective moment of the CW law is $q_c (q_c + 2) = \mu^2_{pm}$ and $q_s = \mu_{sat}$. The dashed line indicates the ratio is unity as is the case for localized electrons. The solid line indicates itinerant electrons **(1)**.

Specific exponents from SCR theory and the size of the ordered moment are used as a signature for a clean weak itinerant ferromagnet, to which $ZrZn_2$ (39) and Ni_3Al (40) are good examples. A method is needed in order to extract M_s and χ data from magnetization measurements in a weak itinerant ferromagnet and typically an Arrott plot is applied. Typical itinerant magnet behavior is described by an Arrott plot (41) that takes a simple expansion of the equation

$$H = aM + bM^3 + ...\qquad\qquad\textbf{(18)}$$

that leads to

$$M^2 = M_s^2 + \frac{1}{b}\frac{H}{M}$$

(19)

where $M_s^2 = -a/b$ and $a = 1/\chi$. This gives parallel isotherms in a plot of M^2 vs H/M, where M is the magnetization of the system, H is the magnetic field, M_s is the spontaneous magnetization, and b is a parameter. The y-axis intercept gives M_s for $T < T_c$, and the x-axis gives $1/\chi$ for $T > T_c$. When the intercept is zero, then $T = T_c$. T_c can be defined where M_s and χ cross at zero, and typical critical exponents for $M_s(T)$ and $1/\chi(T)$ can be probed. Small deviations from the Arrott plots are seen for low fields due to domains and disorder. A good example of an Arrott plot is of the weak itinerant ferromagnet, Ni_3Al, as shown in Figure 1.2. It shows straight, parallel lines. The extrapolated spontaneous magnetization, M_s^2, and the extrapolated susceptibility $1/\chi$ for each temperature are plotted as a function of temperature in Figure 1.3 and the critical temperature is extracted when they cross and is found to be $T_c = 44$ K. The extrapolated spontaneous magnetization and susceptibility are plotted as a function of $T^{4/3}$ in Figure 1.3 which shows a good description for the data in the vicinity of the critical temperature.
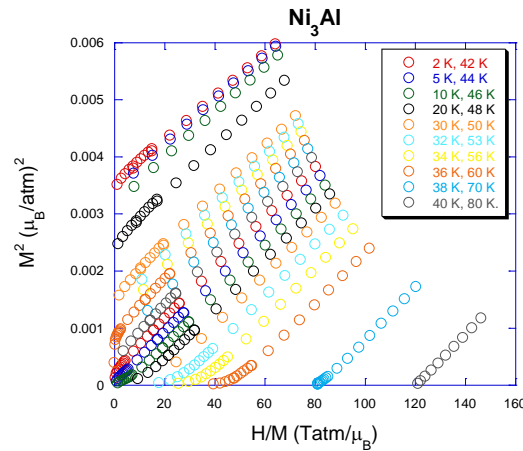
Figure 1.2 An Arrott plot of the weak itinerant ferromagnet Ni$_3$Al at various temperatures.
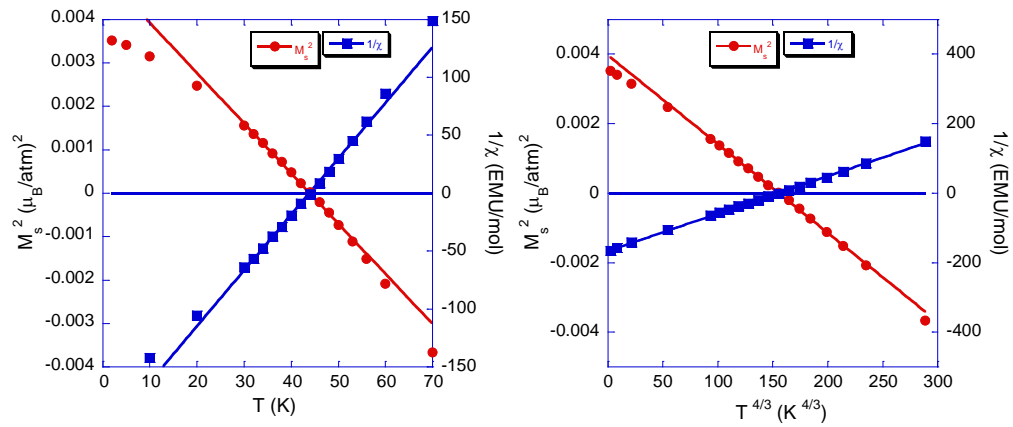
Figure 1.3 (top) A plot of Ni$_3$Al showing the spontaneous magnetization, M$_s$, and the inverse susceptibility, 1/χ, as extrapolated from the AP plotted as a function of temperature, T. (bottom) M$_s$ plotted as a function of T$^{4/3}$

Weak itinerant magnets have interacting itinerant spins and are defined to have a low T$_c$ with spin fluctuations in the region close to the critical temperature. By tuning the interaction further, through e.g., chemical substitution or magnetic field, T$_c$ can be allowed to vanish leading to a non-magnetic ordered state at 0 K. This is an example of a quantum phase transition (QPT), which will be discussed in the next section.

1.2 Classical and Quantum Phase Transitions

In this dissertation, we are studying a ferromagnet with a low critical temperature, T_c, which gets suppressed to zero from dilution leading to a non-ordered state. A phase transition from a magnetically ordered state into a paramagnetic state at 0 K is considered an example of a QPT. While classical phase transitions occur at finite temperatures driven by thermal fluctuations, quantum phase transitions take place at zero temperature as a tuning parameter is changed and are driven by quantum fluctuations. The parameters used to reach the critical regime at zero temperature are pressure, doping, disorder, or magnetic field and change the interaction of the system. The study of this regime is vital in searching for the existence of unconventional behavior in a material, such as superconductivity.

We begin with the order parameter, first introduced by Landau, which characterizes a continuous phase transition, e.g. the onset of ferromagnetism in a zero magnetic field. This thermodynamic quantity is finite in the ordered phase and zero in the disordered phase. For a ferromagnetic transition, the order parameter is the spontaneous magnetization in zero fields in the ordered region, for $T < T_c$. In the disordered region, when $T > T_c$, the magnetization is zero but its fluctuations still exist. As the critical temperature is approached, the fluctuations in a material grow over distance such that the spatial correlations of these fluctuations become long ranged. Very close to the critical point, the length scale, or correlation length, ξ, of the fluctuations diverges as

$$\xi \propto \left| T - T_c \right|^{-\upsilon} \tag{20}$$

ν is the critical exponent of the correlation length. Close to the critical point, the correlation length is the only characteristic length scale of the system. This leads to simple power laws in thermodynamics with related critical exponents which can be found in Table 1.1 below (42). The spontaneous magnetization, M_s, is given when the critical temperature is approached from the ordered regime in zero magnetic field. The susceptibility, χ, the specific heat, C, and the correlation length, ξ, are given when the critical temperature is approached from the paramagnetic regime in zero magnetic fields. The magnetization, M, in a magnetic field, H, is given at the ordering temperature.

Critical Index	Definition	Conditions	
β	$M_s \sim (T_c - T)^\beta$	$T < T_c$	$H = 0$
γ	$\chi \sim (T - T_c)^{-\gamma}$	$T > T_c$	$H = 0$
δ	$M \sim H^{1/\delta}$	$T = T_c$	
α	$C \sim (T - T_c)^{-\alpha}$	$T > T_c$	$H = 0$
ν	$\xi \sim (T - T_c)^{-\nu}$	$T > T_c$	$H = 0$

Table 1.1: Equations of state in the vicinity of a phase transition with critical exponents **(42)**

The most commonly used critical exponents are associated through a scaling relation, (43)

$$\beta\delta = \beta + \gamma \tag{21}$$

β and γ are the critical exponents found from the magnetization and magnetic susceptibility, respectively. The theoretical predictions for the critical exponents can be found in Table 1.2 (42).

The universality of phase transitions, resulting from the diverging correlation length, allows phase transitions from different systems to be described by the same critical exponents. Systems with the same critical exponents are said to be in the same universality class. Renormalization group theory makes predictions about exponents which explain that the thermodynamic properties of a system near a phase transition depend on only a few elements such as spatial dimensionality, d, the number of components of the order parameter, n, and the range of interaction and are independent of specific properties of a system. For example, the 3-d Ising model (42) is in the same universality class as a lattice gas, where both are 3 dimensional, have spin symmetry in one dimension, and have short-range interactions (44).

Critical	Ising Model (n = 1)					FM	Heisenberg (n = 3)	MFT
Index	d = 1	d = 2	d = 3	d = 4	d > 4	Easy Plane	d = 3	
β		1/8	0.31	1/2	1/2	0.33	0.34	1/2
γ	2	1 3/4	1.25	1	1	1.32	1.38	1
δ	inf	15	5	3	3	5	5	3
α		0	0.12	0	0	0.02	-0.1	0
ν	2	1	0.64	1/2	1/2	0.675	0.7	1/2

Table 1.2 Theoretical predictions for the critical exponents near the quantum phase transition **(42)**

The critical behavior of a system depends on dimensionality of the correlation in the material. If the dimensionality of the system is higher than the upper critical
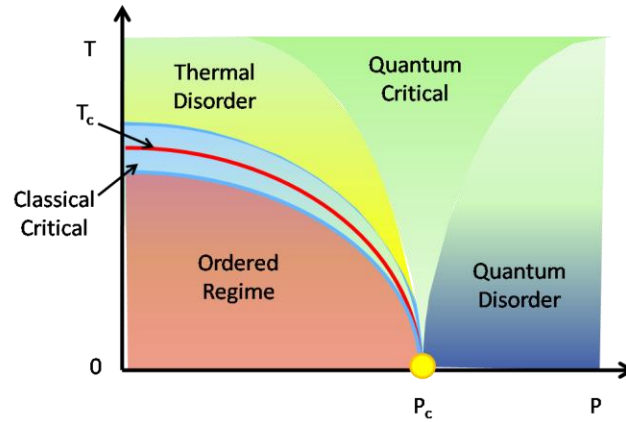
Figure 1.4: Generic phase diagram of a classical and quantum phase transitions. P is a tuning parameter, such as e.g. pressure

dimension, d_c^+, fluctuations are irrelevant and mean-field theory can be used to describe critical behavior. For systems with a dimensionality lower than d_c^+, but higher than the lower critical dimension, d_c^-, ordering still occurs but now the behavior is not described by MFT. When the dimensionality of the system is less than d_c^-, then the system does not order since the order parameter fluctuations are so strong the order is suppressed. For a Heisenberg ferromagnet, $d_c^+ = 4$ and $d_c^- = 2$.

Everything until now is the scenario for a classical phase transition, and since we study a material when its critical temperature goes to zero, we need to look at quantum phase transitions. Here, instead of changing the temperature, we have to change the interaction of the system to drive the order parameter, e.g., an ordered phase to a non-ordered phase at T = 0 as seen in Figure 1.4. While the order parameter is static in the ordered regime, it will fluctuate in the disordered regime. These are quantum fluctuations with the energy scale of the fluctuation rate, $\hbar\omega$, greater than the temperature scale, k_BT. While classical phase transitions are driven by thermal fluctuations, $\hbar\omega < k_BT$, the

quantum phase transitions are driven by quantum fluctuations. At the quantum critical point, thermal and quantum fluctuations compete for $T \rightarrow 0$ and $\hbar\omega \rightarrow 0$ as $k_B T \rightarrow 0$, causing quantum critical fluctuations. The dynamics of the fluctuations are different than for classical phase transitions, they are now critical. Quantum phase transitions can be treated as classical phase transitions by including the dynamics in an extra time dimension, z, leading to an effective dimension, $d_{eff} = d + z$. z is the critical dynamical exponent connecting space and time fluctuations:

$$\xi_\tau \sim \xi^z \sim \frac{1}{\hbar\omega} \tag{22}$$

The critical behavior in the vicinity of the quantum critical point has been recently investigated (2). The fluctuations of an order parameter near a continuous phase transition at zero temperature were first studied by Hertz (45). Using renormalization techniques and by integrating out the conduction electrons from the calculations, he found that both spatial and temporal fluctuations are necessary to determine critical behavior in an effective dimension, $d_{eff} = d + z$, where d is the spatial dimension and z is the dynamical exponent.

It was previously discussed that the magnetization parameters can be extracted through the use of an Arrott plot for weak itinerant systems. However, close to the critical regime deviations might occur and this is no longer possible unless the Arrott plots are modified to yield exponents different than MFT. In probing critical exponents for a quantum phase transition, a modified version of the Arrott plots produces linear isotherms introducing critical exponents, such as γ and β, as found in the equation

$$\left(\frac{H}{M}\right)^{\frac{1}{\gamma}} = a + b \cdot \left(M^2\right)^{\frac{1}{2\beta}} \tag{23}$$

It was originally proposed to describe the magnetization data of nickel near the critical temperature (46). This modified Arrott plot now resembles the original Arrott plot with straight, parallel lines. It is now possible to extract the spontaneous magnetization and extrapolate the susceptibility to obtain a Curie temperature, T_c, and critical exponents from the data. These critical exponents are restricted to the critical regime, where e.g. the correlation length exceeds any lattice parameters. This has been done for the weak itinerant ferromagnetic alloys, $Fe_{90-x}Mn_xZr_{10}$ (47).

The modified Arrott plots are used when near the critical regime. The behavior of the system is also modified in that it differs from Fermi liquid theory for typical metals. This brings us to the next section which gives an overview of Fermi liquid theory and non-Fermi liquid theory.

While QPT can occur in different systems, there is a special interest in magnetic metals. Quantum critical fluctuations can destroy the Fermi liquid scenario which is considered as a robust description for a metal, leading to non-Fermi liquid behavior as addressed in the next section.

1.3 Fermi Liquid and Non-Fermi Liquid

Normal metals are well described by Fermi liquid theory, where electrons are essentially considered as non-interacting quasiparticles treated as fermions. The Coulomb repulsion of conduction electrons can be screened and the scattering probability of electron-electron collisions is very restricted due to the Pauli Exclusion Principle since

electrons are fermions. But for the more localized d electron, Coulomb repulsion is important and with singular interactions occurring close to the onset of e.g. a magnetic phase, the Fermi liquid can be disturbed leading to non-Fermi liquid behavior.

Landau's Fermi Liquid Theory (FL) was originally proposed to describe the low temperature properties of ^{3}He (48) (49). This theory describes the system as though it were a gas of weakly interacting Fermi particles (conduction electrons) obeying the Pauli exclusion principle. The interacting particles are considered as low energy excitations of the interacting system, called quasiparticles, and have an effective mass, m*, due to a screening cloud surrounding it. A one to one correspondence is made between the quasiparticles and the low energy excitations of the non-interacting system (conduction electrons with Coulomb interactions). The notion of mapping this interacting system with a non-interacting one successfully explains systems such as ^{3}He, heavy fermions, and even metals. The physical properties of the Fermi liquid and the free electron gas are similar with the exception of a few parameters, the major one being the effective mass. For example, these properties include the low temperature specific heat, C, magnetic susceptibility, χ, and resistivity, ρ, respectively.

$$\frac{C(T)}{T} = \left(\frac{m*}{m_E}\right)\gamma_0 \quad \textbf{where } \gamma_0 = \left(\frac{\pi^2 k_B^2}{3}\right)N_0(E_F) \tag{24}$$

$$\chi(T) = \left(\frac{m*}{m_E}\right)\frac{\chi_0}{\left(1+F_0^a\right)} \quad \textbf{where } \chi_0 = \mu_B^2 N_0(E_F) \tag{25}$$

$$\rho(T) = \rho_0 + AT^2 \quad \textbf{where } \sqrt{A} \sim m* \tag{26}$$

where F_0^a is an additional Landau parameter and m_E is the free electron mass.

An experimental example of a Fermi liquid is UPt_3 (4) which is a Heavy Fermion compound. These materials are named for the excessively heavy effective masses they incur, on the order of 100 times the electron mass or greater. This is a result of interactions between tightly bound f-electrons and conduction electrons. It has a Curie susceptibility at high temperatures due to the f-electrons behaving like free magnetic moments. These f-electrons interact with the conduction electrons as the temperature is lowered to create the heavy quasiparticles. Weaker interactions between the f-electrons lead to a screening of the magnetic moment at lower temperatures which results in heavier quasiparticles.

Many heavy fermions and also transition metals show deviations from Fermi liquid theory. Fermi liquid theory predicts that the magnetic susceptibility is independent of the temperature, the specific heat coefficient is linear in the temperature, and the resistivity is quadratic in the temperature. The behavior of these quantities now is remarkably characterized by weak power laws or logarithmic divergences towards T→0. The physical properties are found to be as such (6):

$$\frac{C(T)}{T} \propto -\frac{1}{T_0} \ln\left(\frac{T}{T_0}\right) \text{ or } T^{-n} \tag{27}$$

$$\rho(T) \propto T^n \text{ where } 1 \leq n < 2 \tag{28}$$

at low temperature. These power laws can have many origins and it is often the case that non-Fermi liquid behavior is observed close to a magnetic instability, close to a magnetic quantum critical point.

In recent years, for example, compounds such as MnSi and $ZrZn_2$ have been found to violate Fermi liquid theory when magnetic order has been suppressed by external pressure. For example, the resistivity of ferromagnetic MnSi (17) shows a $T^{5/3}$ behavior as $T_c \rightarrow 0$ when under high pressure, which follows the prediction for a quantum critical ferromagnet and differs from the T^2 dependence for a Fermi liquid. Applying theory to derive a quantum critical fluctuation spectrum leads to special non-Fermi liquid theory predictions. More specifically, for a clean 3-d ferromagnet these quantities at very low temperatures are [(7), (22)]

$$\frac{C}{T} \sim -\log T \tag{29}$$

$$\chi \sim T^{-\frac{4}{3}} \tag{30}$$

$$\rho \sim T^{\frac{5}{3}} \tag{31}$$

MnSi and $ZrZn_2$ are good examples but small deviations are still discussed. NFL properties have been experimentally observed close to a magnetically ordered phase as the critical temperature approaches zero. Many systems have been tuned by chemical substitution, by replacing the magnetic ion or the metal host by a different ion. This might change the stoichiometry of the compound and create inhomogeneities which modify the critical behavior. Since it is very difficult to control the degree of "disorder", two extremes can be pursued. While on one hand very "clean" stoichiometric compounds are investigated to be controlled by external pressure, extremely disordered compounds are a completely different scenario. The impact of disorder in a quantum phase transition has been studied recently (19) and disorder brings on stronger quantum fluctuations,

changing the physics of the critical point and the surrounding area. Unconventional behavior is predicted to evolve with disorder that has yet to be experimentally discovered in weak itinerant ferromagnets. So if one were to introduce disorder in a somewhat clean material, would the phase transition be sharp or will it smear? What new phases can be found? Will it follow the same physics as the clean material? To answer these questions we must first take a look at the region where the critical temperature goes to zero under the effect of disorder.

1.4 Influence of Disorder on Phase Transitions

1.4.1 Harris Criterion

The influence of disorder on a quantum phase transition is extremely important and leads to very interesting phenomena. If a system is too inhomogeneous, a phase transition can be suppressed or changed. Harris (50) developed a criteria for the stability of a classical phase transition of a homogeneous system when a small amount of disorder is introduced. He proposed to consider the inequality

$$\nu \geq \frac{2}{d} \tag{32}$$

where ν is the correlation length exponent and d is the dimensionality of the system. If a clean critical point fulfills this inequality, then it is stable against disorder. Otherwise, it is unstable and the critical behavior is modified into three possible scenarios: 1) the system must go to a new different critical point which satisfies the inequality and

becomes stable, 2) the system will obtain a new unconventional critical point, or 3) the phase transition is destroyed.

1.4.2 Percolation Theory

Simply diluting a magnetic site by replacing it by a nonmagnetic site might lead to a percolation transition, which separates a magnetic ordered phase from a nonmagnetic phase where clusters are disconnected. Consider two neighboring magnetically ordered sites, i and j, which can couple either directly or indirectly where the sets of jointly connected sites form clusters with dimensionality, d, (3). The creation of disconnected clusters may result from either bond percolation or site percolation. The clusters connect with one another through bonds and removing bonds between the connected clusters occurs with a probability, p, and creates disconnected clusters. Site percolation may occur when enough "holes" are introduced to isolate a cluster from the rest of the clusters, resulting in it being disconnected. To facilitate a comparison, we use a p as the probability to find the non-magnetic site, which could correspond to our vanadium concentration, x.

There exist three percolation regions for the clusters with different sizes, corresponding to a generic phase diagram of percolation, p, as a function of temperature in Figure 1.5. For $p < p_c$, one may find large connected clusters. At the critical percolation, $p = p_c$, there is a large amount of clusters with a wide range of magnitudes. For $p > p_c$, there are independent clusters.

Assuming there are short range interactions between the clusters, p_c depends on the nearest neighbors, z_{nn}. For a 3-d ferromagnet, predicted values for the bond percolation threshold occurs at $p_c = 0.9$ and for the site percolation threshold is at $p_c = 0.8$. In changing p, the universal critical exponents, ν_p, β_p, and γ_p, can be derived exactly in 2-d and by approximation in 3-d, and correspond to the correlation length, ξ, the mean cluster size, S, the magnetization, M, and the susceptibility, χ in 3-d.

$$
\begin{aligned}
\xi &\sim \left(p_c - p\right)^{-\nu_P} & & & \nu_P &= 0.9 \\
S &\sim M \sim \left(p_c - p\right)^{\beta_P} & &\text{with} & \beta_P &= 0.4 \\
\chi &\sim \left(p - p_c\right)^{-\gamma_P} & & & \gamma_P &= 1.8
\end{aligned}
\tag{33}
$$

(43); (19)

A path along the critical phase transition line can be taken to approach p_c to describe the temperature dependence of the of the percolation

$$
T_c(p) \sim \left(p_c - p\right)^{\phi}
\tag{34}
$$

The exponent, ϕ, is on the order of 1 for 3-d. The thermal exponent of the phase transition close to p_c results in similar values, e.g., $\chi \sim (T - T_c)^{-\gamma_T}$, with $\gamma_T = 1.8$ for 3-d but is very different from the clean classical phase transition, $\gamma = 1.38$ for a 3-d Heisenberg.

Classical percolation theory is not a good description for the location of a quantum critical point in Ni-V since it treats geometric criticalities and related thermal criticalities, but does not include quantum fluctuations expected close to a QCP. Vojta (51) compares the quantum phase transition driven by percolation at p_c with the clean quantum critical point at g_c and the mutual influence of dilution, p, and quantum fluctuations, g. A phase diagram is shown in Figure 1.5.
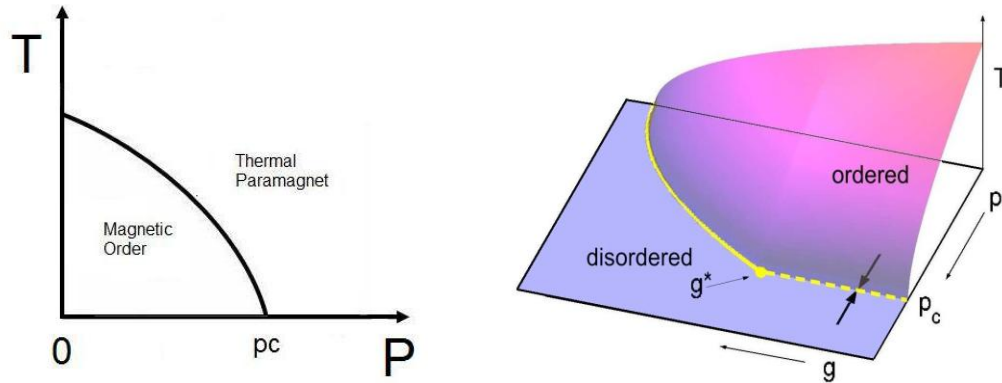
Figure 1.5: a) Generic phase diagram of temperature as a function of probability showing the percolation threshold separating the magnetically ordered phase from the thermal paramagnetic phase. b) Generic phase diagram of the percolation scenario including a quantum fluctuation strength, g, as another dimension **(51)**.

The percolation exponents are already modified at low g at the quantum critical point, p_c, compared to a classical phase transition. They include the critical dynamical exponent, z, through the effective dimension, $d_{eff} = d + z$. The value of z depends on the impact of the conduction electrons on the spin fluctuations. In the case of an insulator, z_0 = 1 will lead to a change of the critical exponents to e.g., $\gamma = 4$ while β remains 0.4 (24). But for the case of a metal where $z_0 = 2$ is expected, the usual exponents are not defined (for example, $\gamma \rightarrow \infty$) leading to a new quantum critical point at g* called an infinite randomness quantum critical point (IRQCP). This new QCP has new critical properties. It is, for example, accompanied by a Griffiths' phase which shows a range of non-universal power laws and not specific universal critical exponents as discussed in the next section.

1.4.3 Griffiths Phase

Disorder is expected to have stronger effects on quantum phase transitions than it does on classical phase transitions. In general, disorder decreases the critical temperature, T_c, from the critical temperature in a clean system, T_c^0. In the temperature range of $T_c < T < T_c^0$, random large, impurity-free regions displaying local order exist with a small probability while the bulk system is still completely disordered. The probability of the existence of these rare region clusters exponentially decreases with its size. Griffiths (52) was the first to show that 'local moments' or 'instantons', induced order parameter fluctuations, are non-analytic in the free energy for this Griffiths region. Although this is typically a weak effect, the singularity in the free energy is stronger in quantum systems than it is for classical systems. Therefore, this influences the physics close to the phase transition in the disordered phase.

When a disordered system is close to a quantum phase transition, the probability, p, that large, rare clusters exist with a distribution of the cluster size, L^d, is found in an exponential form (e.g. in a percolation scenario). The larger a cluster, the more unusual it is to find one.

$$P\left(L^d\right) \sim \exp\left(-cL^d\right) \tag{35}$$

The net magnetic moment for each ferromagnetic cluster is proportional to its size and could quantum tunnel, or fluctuate, between states. The relevant energy scale of the clusters, Θ_L, tells of the fluctuation rate due to the interaction between the clusters of size L^d and is given by the following expression

$$\Theta_L \sim \Theta_{L0} \exp\left(-bL^d\right) \tag{36}$$

The constants c and b are non-universal exponents. The distribution of the energy scale of the clusters $P(\Theta_L)$ becomes a power law distribution which is of the form

$$P(\Theta_L) \sim \Theta_L^{\alpha-1} \text{ where } \alpha = \frac{c}{b} = \frac{d}{z'} \tag{37}$$

The value d is the space dimensionality and z' is seen as an effective dynamical exponent. According to the expectations for a magnetic Griffiths phase, the low field susceptibility χ_0^{-1} and the specific heat, C_s, should then portray a power law with exponent $(1 - \alpha)$, and α_H is obtained from the magnetization plots as a function of field, M(H).

$$\chi_0 \sim \frac{C_S}{T} \sim \frac{1}{T^{1-\alpha}} \tag{38}$$

$$M(H) \sim H^{\alpha_H} \text{ for high field H} > \Theta \text{ where } \alpha = \alpha_H \tag{39}$$

The exponent α is not universal. Instead, it depends on the cluster distribution and the origin of the cluster interaction. The requirements of a Griffiths' phase are an exponential distribution of cluster sizes and a related fluctuation rate causing simple power laws in the thermodynamics. We can pose a question: Can this be realized in a diluted magnetic alloy?

Griffiths' phases are associated with a new infinite-randomness quantum critical point and indeed have been predicted for diluted Ising systems, where the Θ_L is the rate of the fluctuating spins. The tunneling rate of many Heavy Fermion systems can be considered having Ising symmetries and much attention has been drawn to them depicting a possible quantum Griffiths phase since some show power laws in C/T and χ towards low T (53). However, this has been debated (54) because Griffiths' phases result

only when there is weak coupling between the conduction electrons and the spins, giving rise to little or no damping. Since Heavy fermions are metals, the damping effects by the conduction electrons on spin fluctuations are strong. This forces the spins to stop tunneling, leading to a smeared phase transition instead of a Griffiths phase.

The scenario is different in Heisenberg systems with continuous spin symmetry. Here a quantum Griffiths phase is expected in disordered itinerant Heisenberg systems close to the phase transition (55). The clusters cannot freeze individually, instead, they keep fluctuating heading towards a $T = 0$ instability. To understand why an infinite-randomness quantum critical point in a metallic system with a Griffith' phase is expected with a Heisenberg system and not an Ising system, Vojta (24) classified the scenario by comparing important dimensions. A system can only order if its dimension, d, is above the lower critical dimension, d_c^-. For quantum phase transitions, the "space" dimension is increased by the extra "time" dimension, given by z, resulting in an effective dimension, $d_{eff} = d + z$. The finite clusters have no significant space dimension and could not undergo a classical phase transition. But if z somehow exceeds d_c^-, then it can order in a quantum phase transition by developing long range correlations in time. Since the clusters are created by static defects, this is possible. z describes how the dynamics of spin fluctuations propagate in space, which is affected significantly by conduction electrons. In a metal, the expected value of z is 2. For Heisenberg systems with $d_c^- = 2$ ($d_{eff} = z = d_c^-$), the effective dimension is just at the lower critical dimension, while in Ising systems
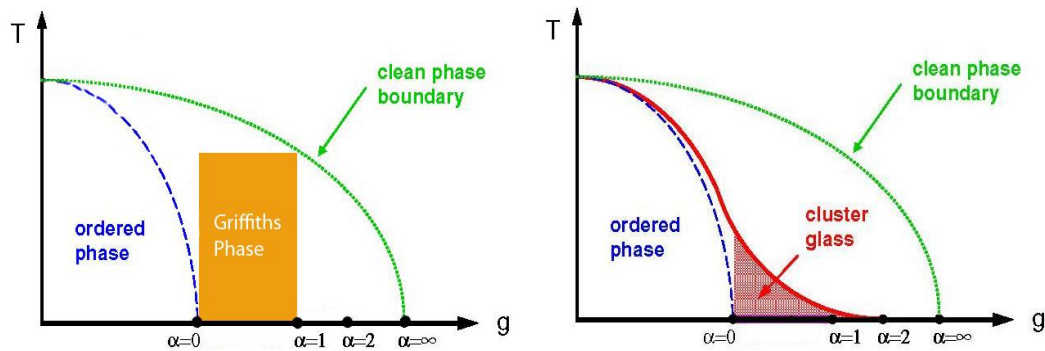
Figure 1.6: Generic phase diagram a) showing a quantum Griffiths' phase for the case of a Heisenberg system at the lower critical dimension, $d_{eff} = d_c^- = 2$ b) a cluster glass phase suppressing the Griffiths' phase in the quantum Ising system above the lower critical dimension, $d_{eff} = 2 > d_c^- = 1$ **(56)**.

with $d_c^- = 1$, the effective dimension is greater than 1 which allows the rare region to order individually.

Figure 1.6, (56), shows two generic phase diagrams for this with temperature, T, as a function of the critical parameter, g, marking the values of the critical exponent, α. Here, g is now a combination of p and g as discussed previously and it corresponds to our dilution parameter, x. The diagram in Figure 1.6 a) is the expected case for the Heisenberg system at the lower critical dimension where $d_{eff} = d_c^- = 2$. Here a quantum Griffiths phase is present in the region bound where the critical exponent $0 < \alpha < 1$, and extends up to the boundary of the clean phase boundary. The diagram in Figure 1.6 b) shows the expected case for the quantum Ising system where the Griffiths' phase is suppressed by a cluster glass phase which is separated by an exponentially decreasing smeared phase transition. This occurs when the system is above the lower critical dimension $d_{eff} > d_c^- = 1$.

This brings the reader to the end of chapter 1, the overview to the theory behind weak itinerant ferromagnets and disorder. The next chapter focuses on the experimental methods for Ni-V.

Chapter 2

Experimental Overview

This chapter deals with the experimental portion of the dissertation. In the lab, I was able to create all of the polycrystalline samples through the use of various apparatus. However, prior to conducting the various research projects, a complete laboratory set up was required. I created a sample growth facility which included a material preparation area, a glove box, an arc melting system, and a tube furnace. The material preparation area was where the samples were weighed and cut and it included a scale and a vacuum sample chamber where samples were stored, which had pressure gauges and was attached to a vacuum pump. The glove box and the arc melting system required vacuum pump and argon gas attachments, which required stainless steel piping and oxygen and moisture traps. An oxygen sensor was placed in the glove box on a homemade acrylic stand.

I grew all of the polycrystalline samples of various Ni-V concentrations to conduct the research required for this dissertation. I also grew many samples that were used for test purposes: $CePd_2Si_2$, $CeCu_6$, Ni_3Al, $Ni_{2.5}Pd_{97.5}$, $Ni_{45}Cu_{55}$, and samples that were potential study interests: $Ce(Ni_{10}Pd_{90})_2Si_2$, $Ce(Ni_{15}Pd_{85})_2Si_2$, $CeAuGe$, $CeAu(Ge_{90}Si_{10})$, $(Ce_{90}La_{10})AuGe$. There were also samples made that were used in neutron scattering experiments using nickel with isotope 58: $Ni^{58}_{88.88}V_{11.11}$ and

$Ni^{58}_{87.75}V_{12.25}$ and samples created for a colleague that were used in neutron scattering experiments and SQUID measurements, respectively: $CeNi^{58}_2Ge_2$, $CeNi_2Ge_2$. Not all of the samples I made were tested, especially since I made two identical of each concentration. Over all, I have made over 150 samples.

All of the samples were grown from pure elements and all that were tested were annealed afterwards. Structural characterization of the materials was performed. DC and AC magnetization experiments were conducted, and the latter was conducted in the environment of a dilution refrigerator as were some of the transport measurements.

2.1 Sample Preparation

The Ni-V samples were prepared from nickel slugs with 99.995% purity and vanadium wire with 99.8% purity purchased from Alfa Aesar. The samples were formed by weighing the nickel slug using a Fisher balance, with precision up to 5 significant digits, and calculating the vanadium weight depending on the concentration of the sample. The formula used for this is

$$m_v = m_{Ni} \cdot \frac{M_v}{M_{Ni}} \cdot \frac{c_v}{c_{Ni}} \tag{40}$$

where m_v is the vanadium mass, m_{Ni} is the nickel mass, M_v is the vanadium molar mass ($M_v = 50.9415$ g/mol), M_{Ni} is the nickel molar mass ($M_{Ni}=58.6934$ g/mol), and c_v and c_{Ni} are the vanadium and nickel concentrations, respectively. The vanadium wire was cut using non-magnetic copper beryllium cutters and weighed within 0.1% accuracy to the intended calculated weight. After melting, spherical samples were created with diameters ranging from 2 - 4 millimeters. Each sample is weighed and the mass after melting is

checked against the total mass of the materials before melting. The uncertainty in the concentrations for vanadium content is on average a maximum of 0.041%.

2.1.1 Mini Arc Melting System

The melting of the Ni and V components is done with the use of the Mini Arc Melting System (MAM-1) made by Johanna Otto GmbH, with a high voltage electric arc. The basic principle is that a low pressure inert gas, e.g. argon, is in a melting chamber separating two electrodes made of tungsten and becomes ionized by the high voltage between the main electrode tip and the secondary electrode. The high voltage ignites the arc when the main electrode touches the second electrode and the arc flows through the ionized argon gas. The arc produces a high intensity light and the high temperature of the arc is hot enough to melt metals and so this process will be used to create the Ni-V samples.

The materials are placed in a water-cooled copper plate in the arc lamp, sealed to the melting chamber, and a purging process begins by alternating vacuum (down to 1 mbar) and argon gas. Argon is chosen to be used for its purity and low thermal conductivity. The argon gas is 99.999% pure and is fed through ¼" stainless steel lines into moisture and oxygen traps to further cleanse it. Approximately four cycles of purging is done using a Leybold Trivac B oil-sealed rotary vane pump, and the final atmosphere is argon at ambient pressure.

The current flows through a conical tungsten electrode tip that is manually controlled with an isolated knob and has 360 degree in-plane movement within the chamber. The arc is ignited by touching the conical tip to an anode tungsten pin

embedded in the copper plate with a current of 100 Amperes. The intensity of the arc is determined by the strength of the current. This is controlled by a potentiometer that varies the current from 5 to 200 Amperes. The samples are always melted at a low current (up to about 50 Amps) as to not lose mass by overheating.

Once the arc is lit a tantalum cylinder is melted insuring that any leftover oxygen in the chamber is absorbed within the metal. Each sample is then melted on each side a total of three times to ensure their homogeneity. They are then weighed and a mass loss calculation is made in comparison with the total element mass before melting.

An ideal sample would not lose mass, however, that is not realistic since some mass is lost during the growing process, depending on the vapor pressure of the material. Two samples of each concentration were always created together and the sample with the lowest mass loss was chosen to continue with the experiments. Typical mass loss percentages ranged up to 0.5% although some samples with mass loss up to 0.9% were accepted for use. However, the samples chosen for the experiments had a maximum error in the vanadium content of 0.041%. Once a sample is chosen it is ready to be annealed.

2.1.2 Annealing

To improve the homogeneity after melting, the samples were annealed to eliminate defects and improve the atomic distribution. We do not have direct evidence but magnetization measurements show a difference between the samples as grown, or non-annealed, and after annealing at different temperatures. Plotting the magnetic susceptibility as a function of temperature shows the transition at the Curie temperature into the ferromagnetic ordered state at low temperature. Annealing leads to a sharper transition and a lower value for the Curie temperature. In the case of e.g. $Ni_{89.29}V_{10.71}$, the raw data magnetic susceptibility versus temperature graph (Figure 2.1) shows an increase of the magnetic susceptibility which is shifted towards lower temperature and a decrease in the magnetization upon annealing. All samples shown are annealed for 3 days at 900 °C, unless otherwise stated.

The annealing is performed in the following way. The samples are wrapped in 99.998% pure tantalum foil and one or two samples are placed in a 10 mm inner diameter quartz tube with one end already sealed. The tube is then pumped on using both a roughing vacuum pump and a turbo pump and the vacuum pressure achieved at the pump is on the order of 10^{-5} millibar or better. A gas of mixed hydrogen and oxygen is used to seal the tube while only the roughing vacuum pump is still running. Two tubes can be arranged to fit in the Lindberg/Blue Mini-Mite tube furnace to be annealed together.
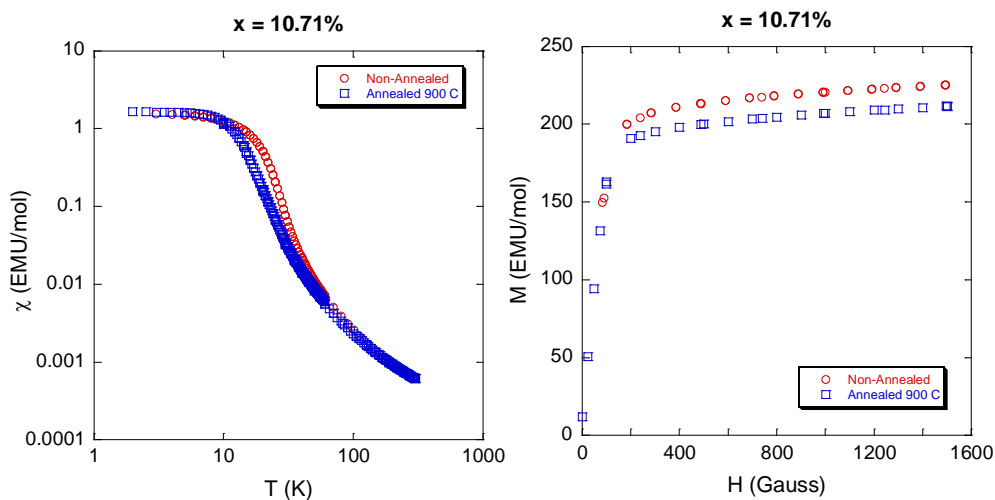
Figure 2.1: a) Susceptibility as a function of temperature and b) magnetization as a function of magnetic field for $Ni_{89.29}V_{10.71}$ to show the difference in magnetic moment response as-grown and in the annealed case.

Most of the samples were annealed at 900 °C for three days. However, two samples at x=11% and x=12.25% were annealed at both 900 and 1050 °C for the same amount of time. The higher annealing temperature gave a sharper transition in the magnetic susceptibility versus temperature and the transition temperature is a lower value for the samples annealed at 1050 °C than at 900 °C. These better results were used for the samples in place of or in conjunction with the lower annealed temperature data.

One must keep in mind when choosing a value that the annealing temperatures must be less than the melting point of the material as to avoid mass loss due to vaporization. Although nickel has a lower melting point than vanadium which is 1450 °C, the maximum annealing temperature chosen for our samples was limited by the specifications of the furnace used.

The samples show a linear decrease in the critical temperature as we increase the vanadium concentration, which is determined from the material growth process. Our plot of the critical temperature, T_c, as a function of vanadium concentration, x, lies in agreement with the data of Bettinelli et al (27), as seen in Figure 2.2. A detailed estimation of T_c will be discussed later. Hence, the methods used for producing and annealing the samples are exceptional and the result is high quality reproducible samples which can be checked through x-ray diffraction.
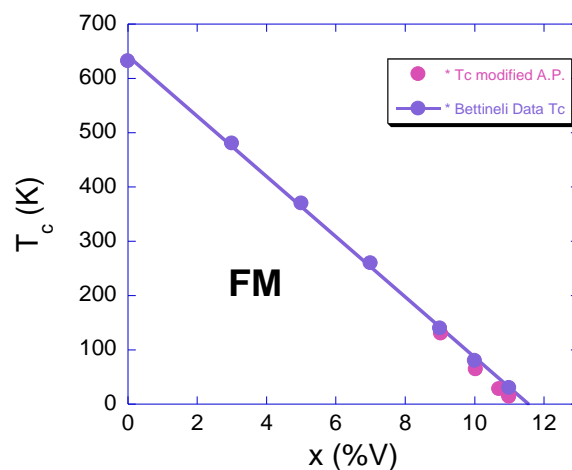
Figure 2.2: Temperature phase diagram showing Tc as a function of vanadium concentration for x = 0 - 12 %.

2.1.3 X-Ray Powder Diffraction

Powder x-ray diffraction is a good method to check the crystallographic structure and to check for other mixed crystallographic phases present in a material. The basic idea is that x-rays diffract from electrons in a crystal lattice as an elastic scattering process causing a constructive interference pattern of sharp peaks in the intensity distribution, called Bragg's peaks (31). Bragg's law states for a constructive interference diffraction peak to occur, then a condition must be satisfied for atoms forming planes separated a distance, d, apart

$$n\lambda = 2d\sin\theta \tag{41}$$

where n is the order of the diffraction peak, λ is the x-ray wavelength, and θ is the scattering angle. It is true for any system as long as i) the angle of the incident beam is equal to the angle of the reflected beam and ii) the diffracted waves produce constructive interference patterns for λ less than or equal to 2d.

The experiments were done using a Siemens commercial x-ray diffractometer with a Cu-Kα beam with a wavelength of 1.5418 Å. The samples were ground to powder using a diamond file, attached to a glass slide using vacuum grease, and were mounted onto the center of the diffractometer. The device is set up such that a θ-2θ scan can be done as seen in Figure 2.3.
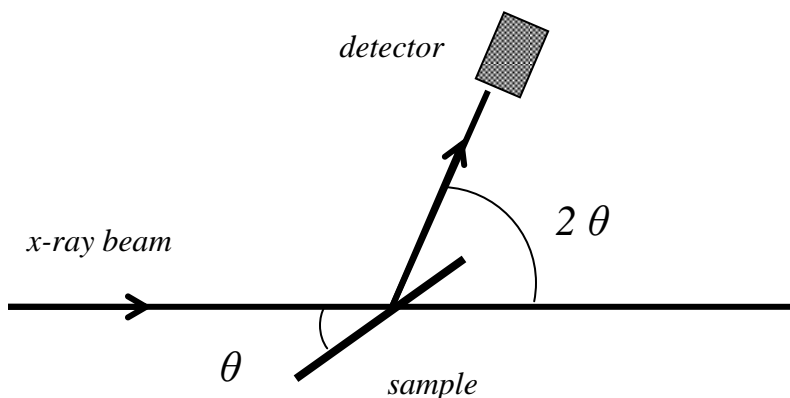
Figure 2.3: Diagram of an X-ray powder θ -2θ scan

The $Ni_{(1-x)}V_x$ samples tested in the diffractometer were vanadium concentration x = 0, 10.71, 11, 11.6, and 13%. The typical scanning angle ranged from a minimum of 35 degrees to 125 degrees with a 5 degree step size. A bump in the background data can be related to the vacuum grease used to attach the sample onto the glass slide.

The Ni-V samples are too ductile to be crushed into powder, so they were ground using two methods. In the first case, I used sandpaper and the structure analysis showed additional Bragg peaks due to SiO. It turned out the sandpaper particles were being loosened during the process and fell into the powder. After this was realized, I used a diamond file for the samples. No additional peaks should have appeared and that was consistent with our findings.

The data was compared with a database of crystal structures and shows a pure FCC material with a single phase. The results of the x-ray diffraction will be discussed in the next chapter.

2.2 Low Temperature Environment

The measurements were done in various temperature environments with two different devices. An evacuated homemade sample stick was used to check the electrical resistivity and the AC susceptibility in temperatures down to 77 K when immersed in liquid nitrogen, down to 4.2 K when immersed in liquid helium, and room temperature measurements. The temperature readings were measured through a Lakeshore Cernox temperature sensor which is more accurate at lower temperatures up to 30 Kelvin, and a Lakeshore Platinum sensor which is used at higher temperatures from about 10 Kelvin to room temperature.

The second device is an Oxford low temperature dilution refrigerator which achieves temperatures down to 50 mK. The temperature was confirmed through the use of an Oxford Ruthenium Oxide temperature sensor being accurate from 0.01 mK – 4.2 Kelvin and the Lakeshore Ruthenium Oxide temperature sensor where the range is from 0.05 to 40 Kelvin.

2.3 Magnetization

There will be two types of experimental procedures used to find the magnetization of a material and these are the alternating current (AC) and direct current (DC) magnetic measurements. In AC magnetization measurements, a small AC drive magnetic field causes a time-dependent magnetic moment in the sample which induces a current that is picked up through induction and could be applied in conjunction with the DC field. With DC magnetization, the same technique applies, only that an external DC magnetic field e.g. from a superconducting coil aligns the magnetic moment of the sample. We used a

SQUID magnetometer for the DC magnetization which has a sensitive superconductive pick-up coil that can pick up magnetic moments up to 10^{-18} T, as compared to 10^{-2} T for an ordinary refrigerator magnet.

Recall from Chapter 1 that the magnetization of a material is proportional to the magnetic moment in some volume, $M = N \mu /V$. Here it is convenient to take the volume as the number of moles in the material, and so $M = m \mu/M_{mol}$ where m is the mass and M_{mol} is the total molar mass of the sample. The total molar mass can be expressed in terms of the molar mass of nickel and vanadium and the vanadium concentration, x

$$M_{mol} = M_{Ni} \cdot (1-x) + M_V \cdot (x) \tag{42}$$

The unit of the magnetization is in EMU/mol which can be converted to Bohr magnetons through the simple relation of 1 EMU/mol $= 1.8e^{-4}$ μ_B/atm.

As with all ferromagnets, a hysteresis is typically present when measuring the magnetization as a function of the applied magnetic field due to the system being magnetized. The magnetization will saturate with an increasing magnetic field and the magnetization remains present in the system even when the magnetic field is reduced to zero. The magnetization data can be demagnetized as a result of the applied external magnetic field, H_a, being different than the internal magnetic field, H_i, of the samples due to a remnant field. When the magnetic field is applied in a particular direction, then the internal field obtained is

$$H_i = H_a - NM \tag{43}$$

M is the magnetization and N is the demagnetizing factor which is dependent on the geometry of the sample. For the Ni-V samples, $N = 4\pi/3$ since they are spherical (57).

The value is consistent with all the Ni-V concentrations with the exception of x = 9.03,

10.03%. For these two sample, the factor N = 4π/3.59 and N = 4π/3.19, respectively.

2.3.1 AC Susceptibility

We choose to study the AC susceptibility since is possible to probe the system at

very low temperatures to obtain more information about the magnetization dynamics of

the system. χ_{AC} is comprised of two parts: a real part, χ' (ω), called the dispersion and a

small imaginary part, χ'' (ω), called the absorption related by the equation

$$\chi_{AC} = \sqrt{\chi'^2 + \chi''^2}$$

(44)

Here, $\chi' = \chi \cos\phi$ and $\chi'' = \chi \sin\phi$, where ϕ is the phase shift between the two

components (58).

The central idea is that a sample sits in a solenoid pick-up coil, consisting of a

small secondary coil inside a large primary coil. An alternating current flows through the

primary coil creating a small AC magnetic field, H_{AC}, also known as the driving field, at

a set drive frequency, ω, that is controlled with a lock-in amplifier. The form of the

driving field in a solenoid is

$$H_{AC} = \mu_0 NI$$

(45)

where μ_o is the magnetic permeability and is equal to $4\pi \times 10^{-7}$ N/A^2, N is the number of

turns in the coil, and I is the input AC current. This driving field aligns the magnetic

moment of the sample with itself which is detected by the secondary coil. In trying to

oppose the field of the sample, an induced voltage is created in the secondary coil that is

comparable to the moment size and this voltage is read by the electronics. The induced voltage is directly related to χ_{AC} by the following relation

$$V_{2_{ind}} = \frac{n_1 n_2 A_2 \mu_0}{l_1} \cdot \omega I_0 \cos(\omega t) \cdot \chi_{AC} \tag{46}$$

where n_1 is the number of turns for the primary coil, n_2 is the number of turns for the secondary coil, A_2 is the area of the secondary coil, l_1 is the length of the primary coil, ω is the driving frequency, and I_0 is the initial AC current.

The solenoid pick-up coil used for these measurements is a homemade creation where the small secondary coil, made from copper wire, is embedded in a larger primary coil which is wound with Nb-Ti wire that is superconducting below 7 K. The spherical sample is implanted in the center of the secondary coil and fixed in place with non-evasive Lakeshore GE varnish. The coil is screwed in place with non-magnetic screws at the end of a homemade copper sample stick that is sealed in a non-magnetic cylindrical brass vacuum chamber. The inner chamber of the sample stick is evacuated to pressures of about 10^{-5} millibar and then dipped in a cryogenic dewar of liquid helium or liquid nitrogen and sealed in place. Helium exchange gas is then introduced inside to allow the inner chamber to cool to the temperature of the surrounding liquid and is administered in 1 millibar increments every 3 – 5 minutes as to not shock the warm sample. Two temperature sensors are mounted near the sample and are used to monitor the temperature of the inner chamber. The sensor mostly used was the Lakeshore Cernox temperature sensor measuring lower temperatures up to 100 K, and the secondary sensor is the Lakeshore Platinum sensor measuring from 10 K to room temperature.

The number of turns for the primary coil is $n_1 = 3850$ turns; the number of turns for the secondary coil is $n_2 = 2120$ turns; the area of the secondary coil is $A_2 = 6.027$ x 10^{-5} m^2; the length of the primary coil is $l_1 = 4.572$ x 10^{-2} m. With these parameters and solving for the susceptibility the following equation is obtained:

$$\chi_{AC} = \frac{71.82}{\omega I_0 \cos(\omega t)} \cdot V_{2_{ind}}$$

(47)

2.3.2 SQUID Magnetometer

SQUID is an acronym for Superconducting Quantum Interference Device which is a very sensitive and highly accurate magnetometer used to measure the strength of the magnetic field in its vicinity. A magnetometer can detect whether a material is diamagnetic, paramagnetic, antiferromagnetic, ferromagnetic, or superconducting. More information can be extracted from measuring the magnetization as a function of temperature or magnetic field, and quantities such as the critical temperature and saturation magnetization can be determined.

The underlying principle is that as a sample moves through superconducting pick-up coils an electric current is induced in the coils from the magnetic moment of the sample. The induced current is sent as an input current to the SQUID electronics where an output voltage is given out that is exactly proportional to the amount of magnetic flux quanta given off from the sample. With a DC magnetic field, the susceptibility is proportional to the magnetization.

$$M = \chi_{DC} H$$

(48)

Over 30 Ni-V samples and over 25 other various samples were tested in the magnetometer over different temperature and magnetic field ranges. The measurements started as a scanning of a particular field, typically at 0.01 T or 0.05 T, at a range of temperature, usually from 2 K – 300 K, and lasted about 2 – 4 hours. These temperature scans were done to reveal the magnetic order of the samples e.g. ferromagnetic and at what temperature the magnetic transition occurs. Further testing was done as field scans, where the temperature was held constant and the scan was done over a magnetic field range, typically from 0 T – 5 T, where each scan lasted anywhere from 1 – 3 hours. The field scans were vital to the nature of the experiment since this data gave the majority of the information for the material.

The SQUID is very sensitive and may pick up signals from materials other than the test sample. In preparing the sample for testing in the SQUID magnetometer, I made sure the workspace and all utensils used are cleaned with alcohol or acetone. Wearing gloves is essential since our skin naturally contains oils that remain on objects when touched.

The sample was made to sit in the bottom half of a vitamin capsule, coated in low temperature Lakeshore varnish and then covered by the top part of the capsule to seal it in place with two pin-head size holes were created in the top of capsule to release air pressure. A new plastic straw is used as the sample holder and two cut pieces from the ends are inserted on either side of the capsule to prevent it from moving. The straw is inserted at the bottom of the measuring probe, which is a made from stainless steel and brass. Initially, the sample was always inserted in the capsule in the same orientation it

was created by the arc lamp. Later measurements of samples oriented at 90 degrees to the typical orientation showed no difference in the magnetization data.

The Lakeshore varnish used is a dissolvable glue that has been tested and shows a moment of $-4e^{-5}$ EMU. The capsule and the straw are both made from a plastic material and were also tested to show a moment of $-3.6e^{-5}$ EMU. These both do not give a significant background signal in the SQUID data.

Inserting the sample

The entrance to the magnetometer sample space is a transfer chamber where the probe is carefully inserted, clamped down and plugged so that no leaks occur while purging or during the experiment. The chamber is purged with helium gas from the helium bath that can be controlled either with the press of a button or through the computer. The system automatically purges three times when the button is pressed once, and it is repeated three or four times. Once the green "ready" button is lit, the valve to the inside chamber is opened and the probe is slowly lowered while rotating to ensure smooth movement. It is crucial to not close the valve at this point as it could pinch the measuring probe.

2.4 Resistivity

The resistance of a material to the flow of current passing through it can tell us about that substance, such as how homogeneous a material is, and the type of scattering centers the electrons scatter from such as magnetic impurities in the material, magnons, and phonons. The temperature dependency of the resistivity in a metal will show different

power laws and can tell us if the material follows Fermi liquid theory or non-Fermi liquid theory. This is important especially when in the vicinity of a quantum critical point.

Resistivity, ρ, is defined from Ohm's law as

$$\rho = \frac{E}{J}$$

(49)

E is the magnitude of the electric field and J is the magnitude of the current density. Experimentally, the resistivity is found by measuring the resistance of a material using the four probe method. Current is applied across the sample, which is ideally a thin wire, and the potential drop across two points on the wire is obtained. The resistance of a resistor can be found from a more common form of Ohm's law,

$$V = IR$$

(50)

The resistance, R, of the four probe method is used to calculate the resistivity, ρ, by obtaining the dimensions of the sample. Their relationship is defined through simple geometry by

$$R = \frac{\rho \cdot L}{A}$$

(51)

where L is the distance between the wire leads measuring the potential and A is the area of the cross-section of the sample. In our case, this is defined as $A = H \cdot t$, where H is the height of the sample and t is its thickness.

The annealed Ni-V alloys were filed down with a diamond file to very thin rectangular shaped pieces, with thickness on the order of 50 μm – 130 μm and a width in the range of 550 μm – 1700 μm. They were glued on cigarette paper, which is a good electrical insulator, with a low-temperature Lakeshore GE varnish on top of a thin copper

plate, a good thermal conductor. Epo-Tek two part silver epoxy was used to glue four copper wires to the sample; two wires being on the outermost part of the sample and the other two were laid out with the maximum amount of distance between them without touching any other contacts and had a contact resistance of 1 Ω. This distance varied each time the sample was mounted and the distances between the inner leads was in the range of 1140 μm – 1340 μm.

The measurements were done in both the dilution refrigerator and a homemade sample chamber. Current flowed through the wires with power being in the nW range and the voltage drop was measured in μV between the two inner wires using the Lakeshore LR-700 Resistance Bridge, which is an AC resistance bridge designed to measure resistance using a various range of low power and voltage. The resistance was measured over a range of temperature from 0.05 Kelvin to approximately 100 Kelvin and at room temperature.

Chapter 3

A Characterization of Weak Itinerant Ferromagnetism in the Transition Metal Alloy: Ni-V

The main chapter of my thesis presents the study of the weak itinerant magnet Ni-V by transport and magnetization measurements. Nickel is an elemental ferromagnet with a high critical temperature of $T_c = 627$ K (59). It is known that replacing Ni with V leads to a strong reduction of T_c (60). At approximately 11% vanadium, the critical temperature goes to zero as shown in Figure 3.1. Beyond the critical concentration, a paramagnet is expected. By tuning T_c, it is possible to probe the typical properties of weak itinerant magnets. This includes specific predictions of critical exponents for a quantum critical point when Tc goes to zero, in particular for a 3-d ferromagnet with itinerant electrons. While many Heavy Fermions close to an antiferromagnetic quantum critical point have been investigated, only a few transition metals were discovered with a low T_c that shows signatures of a ferromagnetic quantum critical point. Recently, the material Ni-Pd with a critical concentration of $x_c = 0.025\%$ Ni was reported to follow the predictions of a clean ferromagnetic quantum critical point (61). Earlier analysis of Ni-Cu or Ni-V show that the paramagnetic side in a phase diagram has complex behavior, unlike that of a simple paramagnet with independent local moments. Beside the band contribution, giant magnetic clusters dominate the magnetic response (28), (62). Earlier resistivity
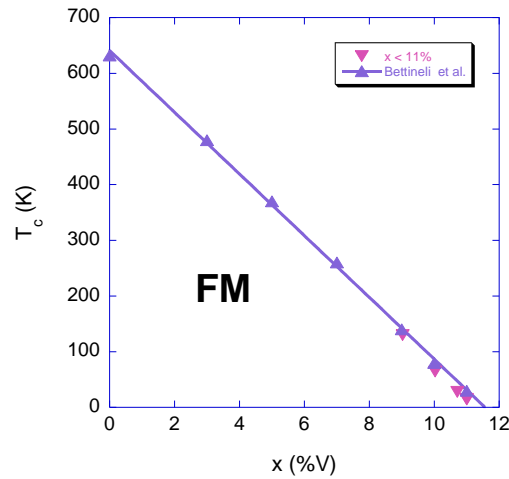
Figure 3.1: Critical temperature, T_c, of $Ni_{1-x}V_x$ as a function of vanadium concentration, x, marking the onset of ferromagnetic order (FM) (**27**). T_c and T* are determined by Arrott plots and modified Arrott plots as explained later in the text.

measurements show unusual exponents in the T dependence, which could be a sign of non-Fermi liquid behavior (28), (25). However, these exponents also do not match the predicted behavior for a 3-d ferromagnet quantum critical point. The residual resistivity, being sensitive to disorder, increases significantly with vanadium concentration as will be discussed in this chapter. Also, the chemical substitution of Ni by V creates large magnetic inhomogeneities throughout the sample as explained later, affecting the magnetic response particularly for x_c and higher concentrations.

Since the magnetic moment distribution of Ni-V alloys is inhomogeneous, we can address outstanding questions of disordered QCP: Would a quantum critical point driven by quantum fluctuations, disorder, or both quantum fluctuations and disorder, still exist? Can we define a critical concentration, x_c? A signature of a weak itinerant ferromagnet is the existence of strong spin fluctuations, so what are the characteristic spin fluctuations

for a strongly disordered system? This present investigation will show that Ni-V presents an example of a disordered ferromagnetic quantum critical point. From the magnetization and transport data, I want to characterize a FM QCP with disorder, reveal the significance of the spin fluctuations, to investigate the critical exponents, and to probe scaling behavior.

3.1 Structural properties

Nickel and vanadium are both transition metals with partially filled d-shells. For a chemically diluted compound, as in this case, the addition of the larger vanadium atoms (pure vanadium is body centered cubic (BCC)) changes the neighbor distances and may change the structure. Hence, it is necessary to check the diluted material and see how consistent the chemical structure of main ingredient, nickel, remains.

Nickel is a face centered cubic structure (FCC) with a lattice constant of a = 3.520 Å at 300 K and the structural properties of pure nickel are preserved with the addition of V and continues up to x = 42% (63). Five samples (x = 0, 10.71, 11, 11.6, 13 %) were filed down to powder and tested in a powder x-ray diffractometer at room temperature. Bragg peaks were found for all of the samples and their Miller indices in consecutive order were (111), (200), (220), (311), and (222), as seen in Figure 3.2 a) for samples x = 0, 11, 13%. This crystallographic structure was confirmed to be single-phase FCC for all the samples, since no extra reflections could be resolved and the intensity ratio remained constant. The inset of Figure 3.2 a) shows the addition of vanadium causes an increase in the peak widths as compared with pure nickel, showing a distribution of lattice constants, and a shift in the peak maxima. The position of the maxima will allow a calculation of the
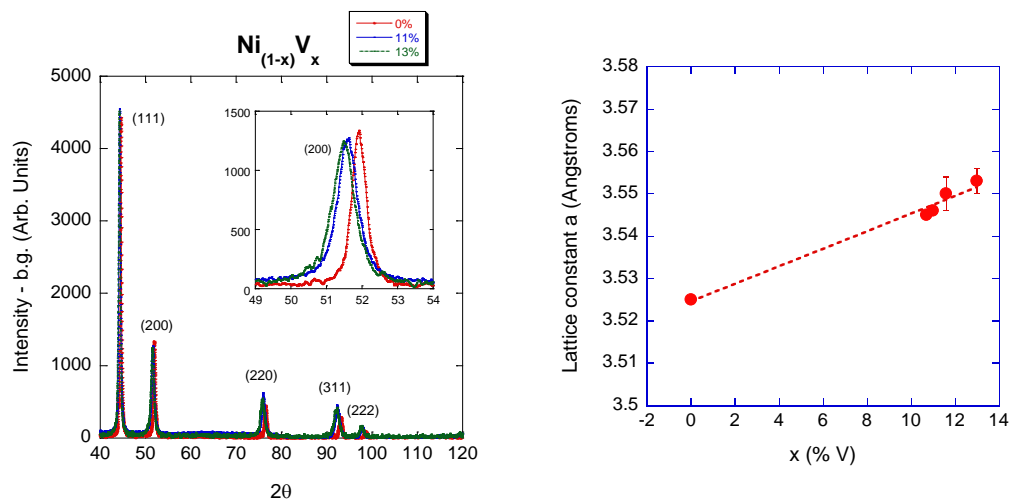
Figure 3.2: a) Relative intensity minus a background as a function of the scattering angle, 2-θ, for Ni-V showing peaks with Miller indices of (111), (200), (220), (311), and (222). Inset is a close up of the (200) peak b) Lattice constants of an fcc lattice of Ni-V alloys as determined from X-Ray powder diffraction

lattice constant which shows a small increase of about 0.7% per 0.8% vanadium as compared with pure Ni with a = 3.520 + 0.028 Å, as seen in Figure 3.2 b). Perhaps the larger lattice constant would be primarily due to the addition of the vanadium atoms, since they occupy 20% more volume comparing with the nickel atoms (31).

The increase of the peak width as compared with nickel shows that the samples become more disordered as the nickel is diluted, but each concentration remains with an FCC structure.

3.2 Resistivity

One of the first signs of NFL behavior can be seen in the resistivity. In particular, the resistivity in the low temperature regime close to a possible critical point deviates from the typical T^2 dependence. From previous magnetization studies (25), the critical concentration of Ni-V where $T \rightarrow 0$ is estimated to be $x_c = 12.8\%$, and resistivity measurements reveal unconventional power law behavior in that regime for $x > 11\%$.

The temperature dependent resistivity for low temperatures takes the form

$$\rho(T) = \rho(0) + AT^n , \tag{52}$$

where $\rho(0)$ is the residual resistivity (at $T = 0$ K) and A is a constant called the resistivity amplitude. The power, n, is the smallest and the constant, A, is the largest around the critical concentration when the resistivity is fit as a function of temperature.

The power of n changes with the type of scattering center found in the material and with the temperature regime being probed. A typical FL with a well defined quasiparticle-quasiparticle scattering would have a power of $n = 2$, and a power of $1 < n < 2$ indicates NFL. In the magnetic ordered state, electron-magnon scattering is expected leading to powers usually higher than or equal to 2 which is dependent on spin wave dispersion, anisotropy, and damping. At the quantum critical point the resistivity for a clean ferromagnet is proportional to $T^{5/3}$ whereas it is $T^{3/2}$ for an antiferromagnet (22).

Furthermore, the homogeneity of the material can be observed through the residual resistivity, which is the resistivity at zero temperature. Impurities or defects not on the periodic lattice will cause conduction electrons to scatter. A more homogeneous material will have a lower residual resistivity because there are less incoherent scattering

centers. Usually, the resistivity at room temperature, ρ_{RT}, is compared with the residual resistivity, ρ_0, residual resistivity ratio, $RRR = \rho_{RT}/\rho_0$, to exclude errors in the geometry of the material. A lower resistivity ratio usually indicates a more disordered material. Figure 3.3 a) – f) show the resistivity as a function of temperature for our six annealed samples with vanadium concentration x = 0, 9.03, 11.11, 11.6, 12.5, and 15%. Power law fits for Equation (51) in the range of T = 5 - 80 K are made for all the graphs and the resistivity power, n, the resistivity amplitude, A, the residual resistivity, ρ_0, and the residual resistivity ratio, RRR, are all extracted and plotted as a function of vanadium concentration, x, respectively in Figure 3.4 and Figure 3.5. The fit range is restricted to low temperatures, about 1/10 the value of critical temperature of nickel.

For pure Ni, the power n coincides with the expected value for an itinerant ferromagnet within error bars, as seen in Figure 3.4 a). The power n decreases with x to about n = 1 for x = 11.6% and then increases to n = 1.7 for x = 15%, clearly indicating NFL behavior when n < 2, but not exactly the n = 5/3 prediction as expected for a clean 3-d FM quantum critical point. The resistivity amplitude, A, is plotted as a function of concentration (Figure 3.4 b). The data show a maximum at x = 11.8% which agrees within 5% to the critical concentration $x_c = 11.2\%$, where $T_c(x)$ is linearly extrapolated to zero for the Ni-V data, and coincides to within 2% to x = 11.6%, the concentration with the lowest power n, indicating a relationship between the resistivity power and magnetic fluctuations (which will be discussed later.)

The residual resistivity is plotted as a function of concentration in Figure 3.5 a), and it increases as the vanadium concentration is increased. This implies there are more

and more impurities as the vanadium content is increased, leading to a more inhomogeneous material in the electronic distribution. The absolute value has large error bars due to the uncertainty in the geometry of the samples. Note that the value for sample $x = 11.11\%$ is lower than what is assumed from the fit. Perhaps this occurs at this concentration since a stoichiometrically ordered compound is possible with the Ni and V atoms arranged in a particular order (64). The fit through the data points is a guide for the eye. Figure 3.5 b) shows the resistivity ratio plotted as a function of concentration. While the ratio for pure Ni is rather high, the RRR for the alloyed compositions is close to 1 showing Ni-V is disordered. This is expected for a random distribution of vanadium and nickel on FCC lattice sites.

Ni-V is a material that shows signatures of NFL behavior in the temperature dependent resistivity, but the power, n, is lower than what is predicted for a clean FM quantum critical point. Disorder is also indicated by the high residual resistivity. The strongest deviations from FL behavior are in the vicinity of vanadium concentration when Tc approaches 0, signifying that the quantum critical fluctuations are possible scattering centers.
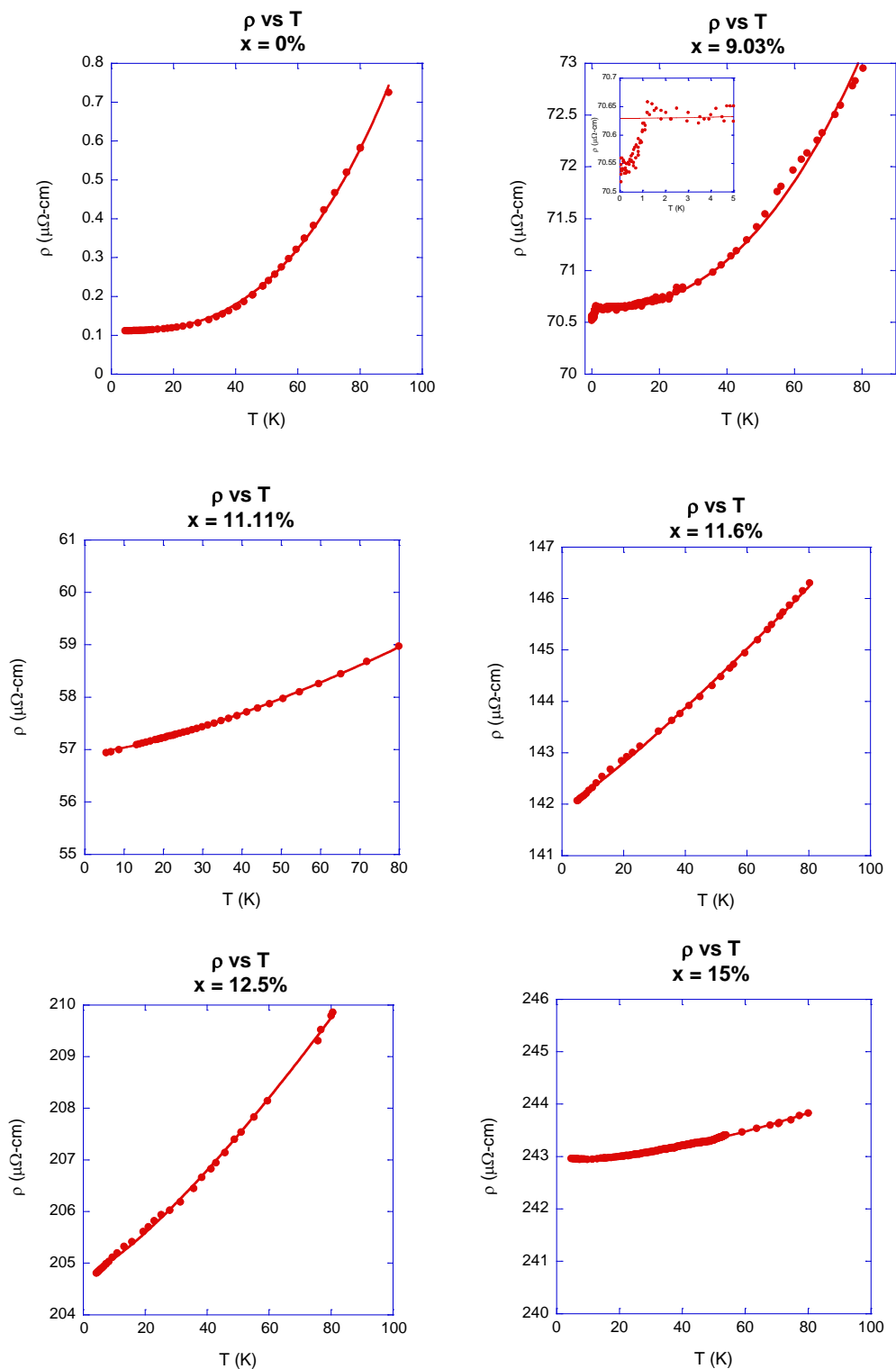
Figure 3.3: Resistivity of $Ni_{(1-x)}V_x$, x = 9.03 − 15% plotted as a function of temperature with power law fits. Inset of x = 9.03% shows a possible onset of superconductivity below 1.5 K, which could be due to small vanadium residue **(82)**.
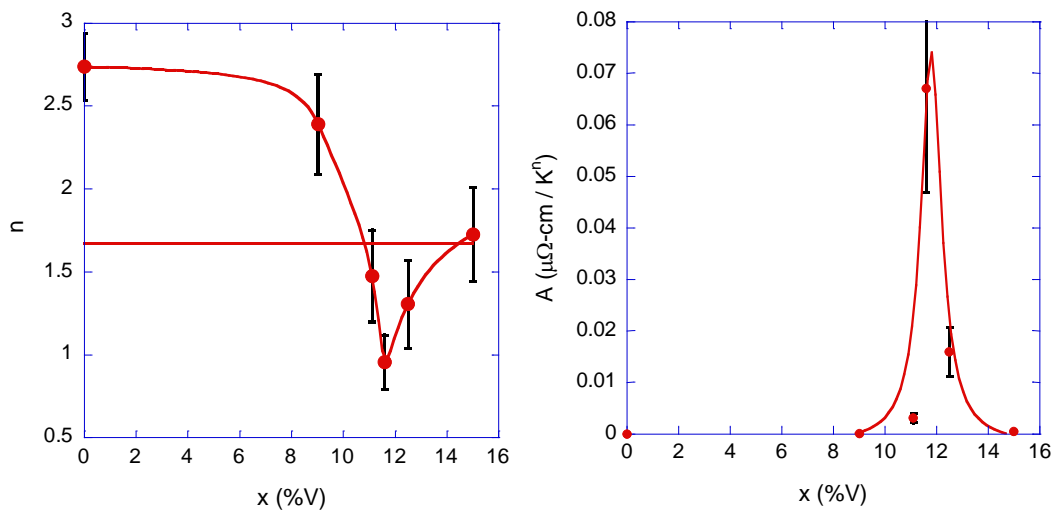
Figure 3.4: a) Power of Resistivity, n, as a function of concentration, x, with a straight line marking n = 5/3. The line is a guide to the eye. b) Resistivity fit parameter A as a function of concentration , x. The line is a guide to the eye.
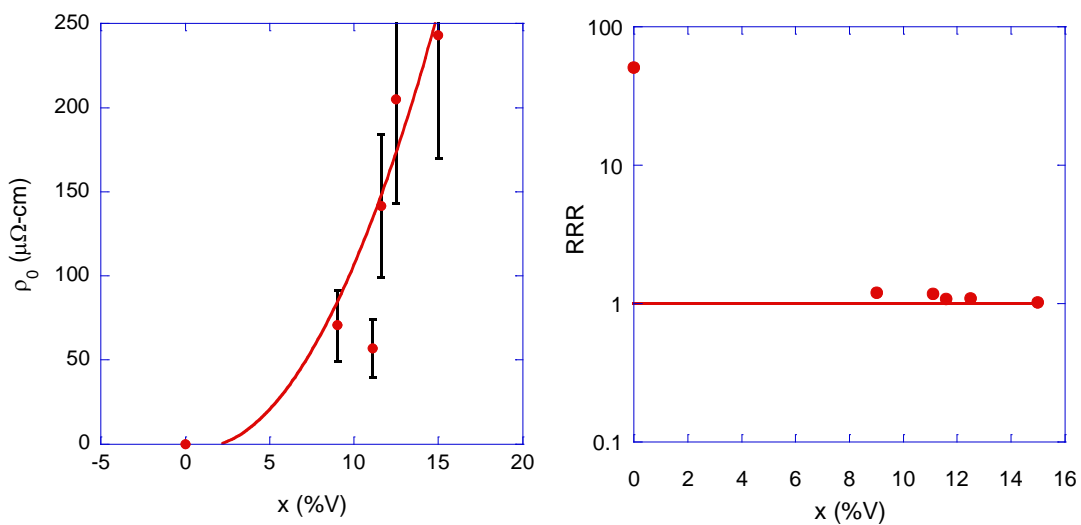
Figure 3.5: a) Residual resistivity, ρ_0, vs x b) Residual resistivity ratio, RRR vs x

3.3 Magnetization Analysis

In the previous sections, disorder in Ni-V has been seen in both the structure and resistivity measurements. Furthermore, signs of NFL behavior are found in the resistivity through power laws. Additional investigations of the magnetization will confirm that Ni-V is a weak itinerant material. The results of the magnetization data in the upcoming sections will investigate the behavior of a disordered quantum critical point (QCP).

The order parameter of homogeneous ferromagnetic order is the spontaneous magnetization, M_s, which is defined as $M_s = M (H{\to}0)$. The onset of ferromagnetism at the critical temperature, Tc, is ideally marked by the onset of M_s and the divergence of the magnetic susceptibility, χ, which is defined as $\chi = dM/dH\big|_{H\to 0}(T)$. Close to the phase transition, critical exponents β, γ, δ, can be determined from M(T), χ(T), and M(H, T_c) including a ferromagnetic order temperature, T_c. A saturation magnetization, M_{sat}, the maximum magnetization in a magnetic field, can estimate a typical moment size per atom or unit cell.

Many characteristics of a ferromagnet can be collected from magnetization measurements in temperature, T, and magnetic field, H. Estimating the spontaneous magnetization and the magnetic susceptibility is usually done in itinerant magnets by using an Arrott plot (46) by plotting M^2 as a function of H/M as seen in Equation (19) from Ch1. The y-intercept value gives the spontaneous magnetization at 0 T, M_s^2, and the x-intercept value gives the value for the inverse susceptibility, $1/\chi$.

A power law is expected in $M_s(T)$ and $\chi(T)$ close to the phase transition at T_c. The spontaneous magnetization and the inverse susceptibility are shown below with the corresponding power law exponents, β and γ, respectively.

$$M_S^2 \sim (T - T_C)^{2\beta} \tag{53}$$

$$\chi^{-1} \sim (T - T_C)^{\gamma} \tag{54}$$

We use the idea of critical exponents and apply it in a wide temperature regime, even though the area is not critical. The exponents can typically be mean field (MFT) and the values for this are $\beta = \frac{1}{2}$ and $\gamma = 1$.

Signatures for a clean weak itinerant ferromagnet include the size of the ordered moment (at saturation) and specific exponents from the Self Consistent Renormalization theory (SCR) (65) which states the spontaneous magnetization and the inverse susceptibility close to T_c are related to the temperature as

$$M_S^2 \sim T^{\frac{4}{3}} - T_C^{\frac{4}{3}} \tag{55}$$

$$\chi^{-1} \sim T^{\frac{4}{3}} - T_C^{\frac{4}{3}} \tag{56}$$

In the next subsections, dc magnetizations studies were done for ten concentrations: $x = 9.03$, 10.03, 10.71, 11, 11.4, 11.6, 12.07, 12.25, 13, and 15% over temperature ranges of $1.8 - 300$ K and in fields up to 5 T.

3.3.1 $Ni_{(1-x)}V_x$ with x < 11%

Magnetization, M, is demagnetized and plotted as a function of magnetic field, H, for different temperatures in the range of 2 − 300 K in Figure 3.6 a), Figure 3.7 a), Figure 3.8 a) and the Arrott plots (M^2 vs H/M) are shown in Figure 3.6 b), Figure 3.7 b), Figure 3.8 b) for samples x = 9.03, 10.03, and 10.71% respectively. It is possible to determine the transition temperature (Figure 3.12 a), T_c, by plotting both the extrapolated M_s^2 and $1/\chi$ as a function of temperature and finding a common temperature, T, where both quantities vanish as shown in Figure 3.9. M_s^2 and $1/\chi$ are fitted to Equations (53) and (54) which are consistent with mean field theory exponents in a wide temperature and magnetic field regime where $\gamma = 1$. The exponent $\beta = \frac{1}{2}$ remains constant for all the samples. The emphasis here was not to measure precise classical critical exponents in a limited critical regime, but to show the overall behavior in a wide T region also beyond the critical regime.

Even though the exponent, γ, for T > T_c follows MFT in a limited T regime, the samples x < 11% are consistent with the SCR theory in β and γ close to T_c in Equations (55) and (56) and are seen in Figure 3.9 b. This signifies that M_s and x are consistent with predictions of a weak itinerant ferromagnet, as expected close to a clean ferromagnetic quantum critical point.

A few comments must be made on the results of this method in obtaining the exponents. The detailed estimate of an exponent strongly depends on the temperature and field regimes of the fit and the choice of T_c. For the lines extrapolated in the Arrott plots, only data in the high field regime of H = 2 − 5 T were used. The spontaneous

magnetization for x = 9.03, 10.03, and 10.71% are fit from $0.39T_c - T_c$, $0.1T_c - T_c$, $0.36T_c - T_c$ and the susceptibility are fitted from $T_c - 1.54T_c$, $T_c - 300K$, $T_c - 1.4 T_c$. An average of the critical temperature was made if T_c from the extrapolations for M_s^2 and $1/\chi$ were not an exact match. Furthermore, not enough data was taken for some of the samples, as seen for x = 10.03% in Figure 3.20. Even though the analysis of the data still worked and we were able to obtain power laws, more accurate values would have been obtained with more data points.
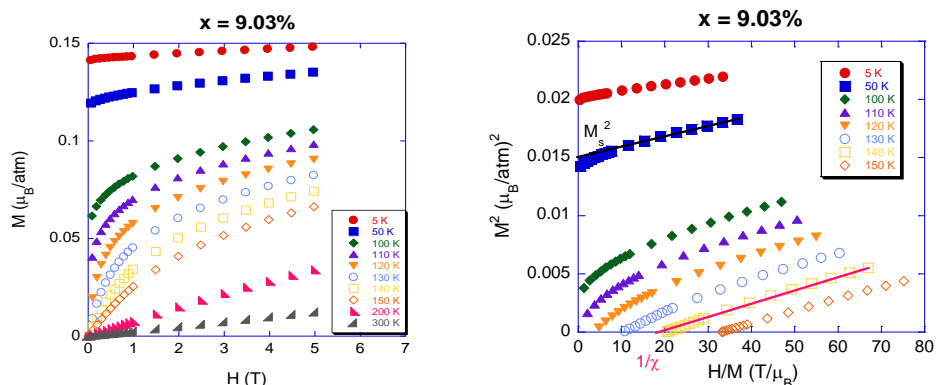
Figure 3.6: a) Magnetization vs magnetic field for Ni$_{90.97}$V$_{9.03}$ in the temperature regime of 5 - 300 K and in magnetic field, H. b) Arrott plot of Ni$_{90.97}$V$_{9.03}$ with temperatures from 5 - 150 K showing the high field extrapolations to the x and y intercepts to obtain the inverse susceptibility and spontaneous magnetization, respectively
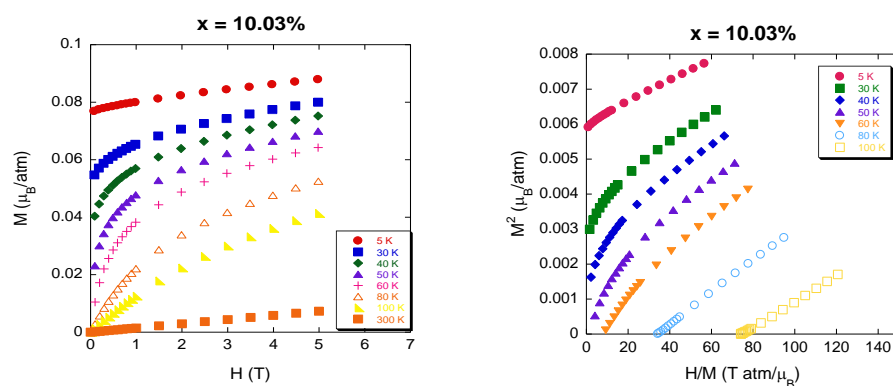
Figure 3.7: a) Magnetization vs magnetic field for Ni$_{89.97}$V$_{10.03}$ in the temperature regime of 5 - 300 K in magnetic field, H. b) Arrott plot of Ni$_{89.97}$V$_{10.03}$ with temperature in the range of 5 - 100 K in fields from 0 - 5 T.
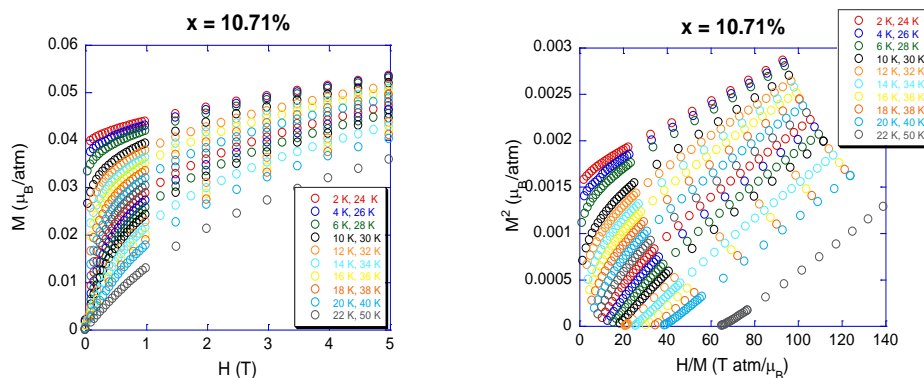
Figure 3.8: a) Magnetization vs magnetic field for Ni$_{89.29}$V$_{10.71}$ in the temperature range of 2 - 300 K in magnetic field, H. b) Arrott plot of Ni$_{89.29}$V$_{10.71}$ with temperature in the range of 2 - 50 K with fields from 0 - 5 T.
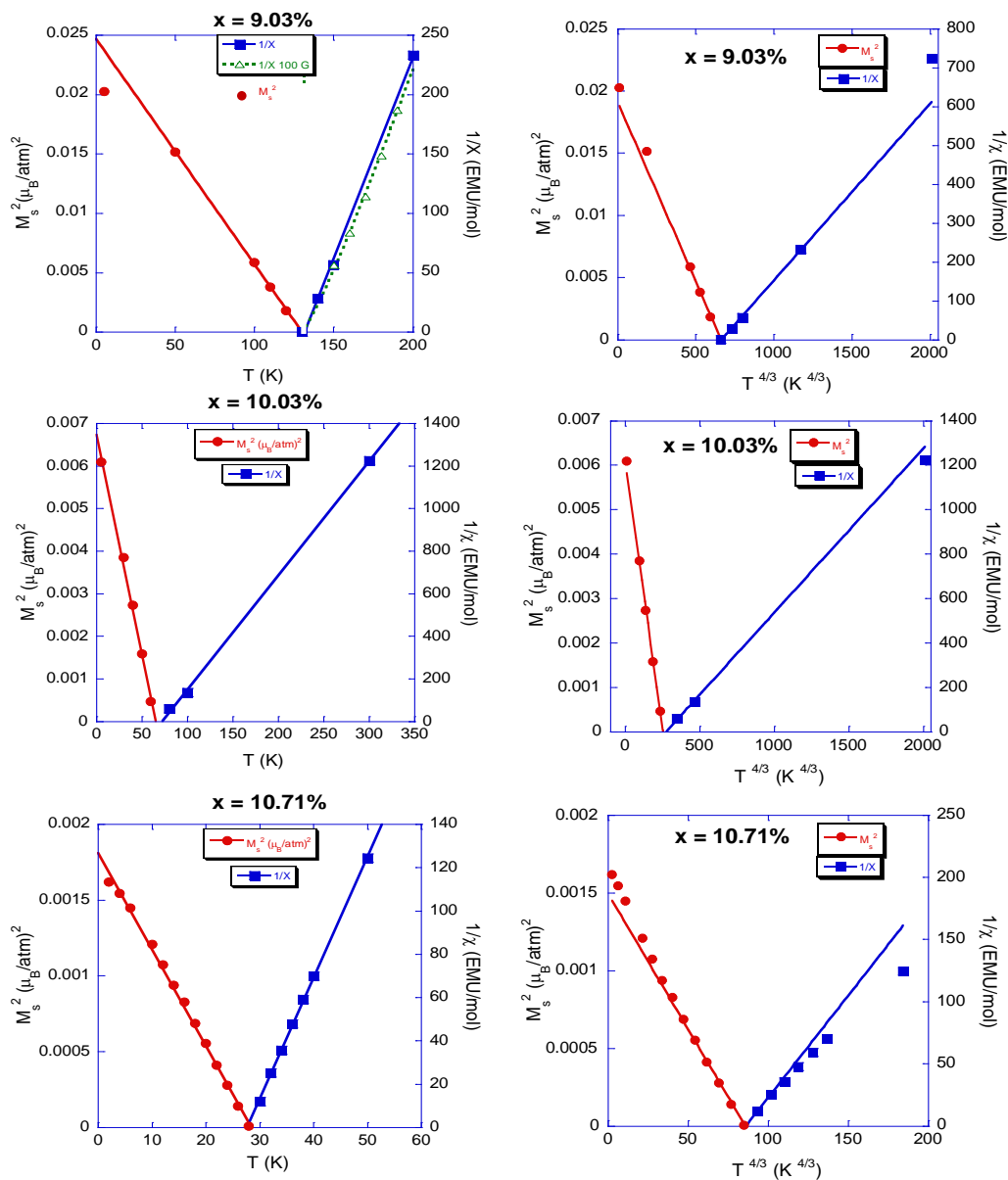
Figure 3.9: a) Square of the spontaneous magnetization, M_s^2, and inverse susceptibility, $1/\chi$, extrapolated from the Arrott plots for x = 9.03, 10.03, 10.71% plotted as a function of T with a linear fit to obtain T_c. The graph for x = 9.03% shows the inverse susceptibility as a function of temperature used to extract the exponent γ. For x = 9.03%, $1/\chi \sim (T-T_c)^\gamma$ is shown including the low field magnetization data at higher temperature, M(T,100G). b) Square of spontaneous magnetization, M_s^2, and inverse susceptibility, $1/\chi$, as extracted from the Arrott plots as a function of $T^{4/3}$. The concentrations x = 9.03, 10.03, 10.71% follow a $T^{4/3}$ behavior in the magnetization and susceptibility in the regime close to T_c.

3.3.2 $Ni_{(1-x)}V_x$ with x = 11%

While the magnetization for x < 11% is well described by the weak itinerant SCR model, the magnetization for x = 11% shows some deviations. The Arrott plot isotherms are still parallel (Figure 3.10 b); however, they are now beginning to become slightly curved at high fields and low temperature. A high field extrapolation to determine M_s is still possible by omitting the low field data. Further samples with higher vanadium content do not follow the Arrott plots and require a slightly modified approach as discussed later.

The analysis in retrieving M_s and $1/\chi$ for x = 11% are the same as for the concentrations x < 11%. An Arrott plot is made and a high field extrapolation, from (2 – 5 T)/M, is taken. The spontaneous magnetization is taken from the y-intercept data, and the inverse magnetic susceptibility is taken from the x-intercept data, as shown in Figure 3.11 a). The sample x = 11% follows mean field theory where its exponents $\gamma = 1$, $\delta = 3$, and $\beta = \frac{1}{2}$ are valid in a wide temperature regime of 2 K to 300 K in magnetic fields of 0.5 T to 5 T. These results can be shown in a scaling plot (Figure 3.11 b) where $M^2/(T-T_c)$ plotted as a function of $H/M/(T-T_c)$. All the data collapse on two curves above and below T_c with different constants, C.

$$\frac{M^2}{T-T_C} = \frac{H/M}{T-T_C} - C_{hi,lo}$$

(57)

For T < T_c, the constant value is -1100 $EMU^2/(Kmol^2)$ and for T > T_c, the value is +800 $EMU^2/(Kmol^2)$. T_c is obtained from the x-intercept of the spontaneous magnetization and inverse susceptibility data and remains finite with a value of 14 K, which is 2% of the T_c

of pure Ni. In the previous section, the spontaneous magnetization and susceptibility of samples 9.03, 10.03, and 10.71% were analyzed in a $T^{4/3}$ behavior close to T_c. This behavior for a clean ferromagnetic QCP does not work well for x = 11%. This indicates enough disorder is present in the material to differ from concentrations x = 9.03 − 10.71%.

Figure 3.12 a) shows T_c decreasing linearly with vanadium concentration and is linearly extrapolated from the critical temperature of pure nickel to obtain a critical concentration of 11.2%. As seen in Figure 3.12 b), the spontaneous magnetization also decreases linearly with vanadium concentration, x, to a critical concentration of about 11.4%. The average spontaneous moment decreases with increasing vanadium concentration as shown in Figure 3.12 b. The exponents γ = 1.14, 1.12, and 0.97 were seen consecutively for x = 9.03, 10.03, and 10.71% in the temperature range of 1.08*Tc to 300 K, in a wide T regime. At this point, one must realize the impact of the vanadium atoms in reducing the magnetic moment and the transition temperature of nickel. It only takes 11.2% of vanadium to reduce the critical temperature of nickel from 627 K to zero and the spontaneous magnetization from 0.6 μ_B to 0.02 μ_B. A potential idea to explain this will be mentioned in a later section.

Since this compound, with x = 11%, is so close to the critical concentration, it was worth investigating how the annealing affected the sample. Two individual annealing processes were done to the same sample. It was first annealed at 900 ℃, where T_c was found to be 15.3 K. The second annealing was at an increased temperature of 1050 °C and a lower Curie temperature was found at 14 K. The higher the annealing temperature, it seems, gives a lower Curie temperature and a lower value for the spontaneous

magnetization which at 5 K is $M_s = 2.04 \times 10^{-2}$ μ_B compared with $M_s = 2.28 \times 10^{-2}$ μ_B for the lower annealing temperature suggesting the samples were more homogeneous and had less chemical clustering. The data for the higher annealed temperature was used unless otherwise stated.

Other concentrations were also annealed and differ to the non-annealed, or "as grown" samples. In general, the spontaneous magnetization and T_c decrease with an increasing annealing temperature resulting in a sharper transition.
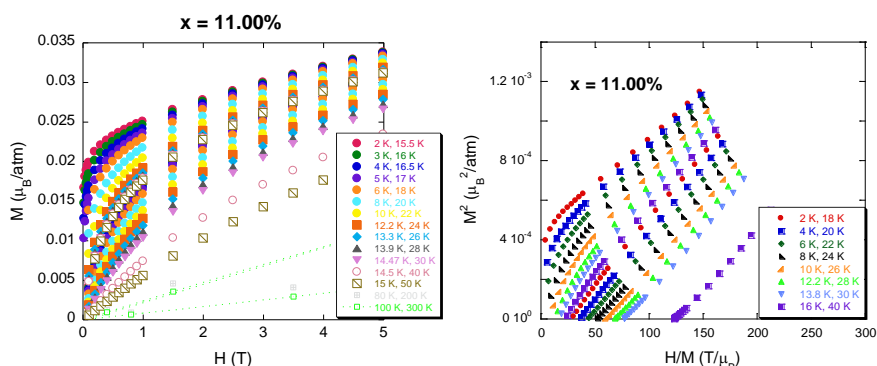
Figure 3.10: a) M vs H plot for $Ni_{89.00}V_{11.00}$ in the temperature range of 2 - 300 K with fields from 0 - 5 T. b) Arrott plot for $Ni_{89.00}V_{11.00}$ in the temperature range of 2 - 40 K with fields from 0 - 5 T obtaining Tc = 14 K with a high field extrapolation in the range from $1.5 - 5$ T.
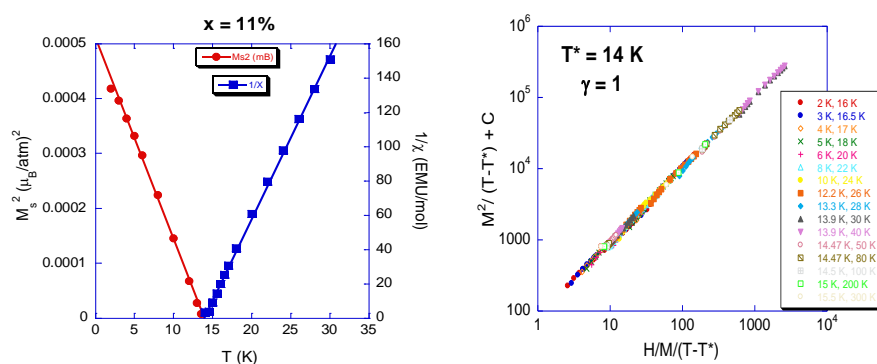
Figure 3.11: Spontaneous magnetization and inverse susceptibility extrapolated from the Arrott plot for x = 11% plotted as a function of T with a linear fit to show $T_c = 14$ K. b) Scaling plot for vanadium concentration x = 11% in the temperature regime of 2 - 300 K in magnetic fields of 0.5 - 5 T with a critical temperature of 14 K. The constant C is -1100 for T < Tc and +800 for T >Tc.
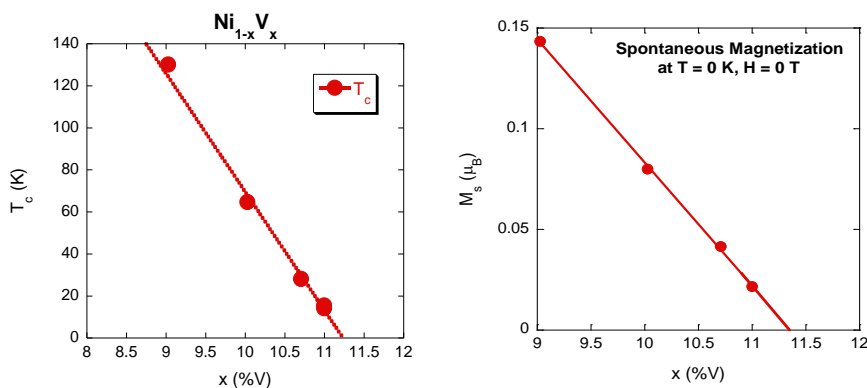
Figure 3.12: a) The critical temperature as a function of vanadium concentration with a linear fit extrapolated to give a critical concentration $x_c = 11.2\%$. b) Spontaneous magnetization decreasing with increasing vanadium concentration where $M_s \sim (x - x_c)$

3.3.3 Ni$_{(1-x)}$V$_x$ with 11% < x < 12%

Figure 3.13 shows M vs H for x = 11.4 and 11.6%. It is not obvious if there is a finite M$_s$ from looking at these graphs. Presenting them in an Arrott plot (Figure 3.14) shows s-shaped isotherms, but a high field extrapolation still yields a finite M$_s$ at low temperatures. Contrary to this, a low field extrapolation would give a negative y-axis intercept stating that this sample does not have ferromagnetic ordering, but it is paramagnetic.

A modified form of the Arrott plots was used to determine classical critical exponents, such as γ and β, as found in the equation below (46).

$$\left(\frac{H}{M}\right)^{\frac{1}{\gamma}} = a + b \cdot \left(M^2\right)^{\frac{1}{2\beta}} \tag{58}$$

This was originally proposed to describe the magnetization data of nickel near the critical concentration. Even though this relation is only valid in a limited critical regime, it has been used to describe, e.g. amorphous materials, outside of the critical regime (66). The use of incorrect powers, partial data sets, and large magnetic fields implies abuse of the Arrott plots and attaining the critical temperature results in a smeared transition in place of a sharp one (67). More specifically, for a weak itinerant ferromagnet such as ZrZn$_2$, it is mentioned these materials follow Equation (57) with powers equivalent to mean field theory, β = 0.5 and γ = 1, but the isotherms in the Arrott plots are not parallel in both a homogeneous and inhomogeneous system.

Some comments are needed at this point in lieu of this debate. While it is true that Arrott plots are used outside of their intended application in this present study, they still

describe the data well, except at very low magnetic fields, and we can still extract useful information from them. In our case, only the critical exponent, γ, was modified from MFT to allow the curvy isotherms to be straight and parallel. All of the data was used for this, including the higher magnetic field data (up to 5 T.) It was mentioned that extrapolating from the higher magnetic field data can lead to a wrong T_c if the data is curved, but our isotherms were straight with this change. The lower field data were not included in the extrapolations. Furthermore, scaling the data provides additional proof of the modified Arrott plots which is seen below. It already shows that it is indeed difficult to really measure the critical temperature in an inhomogeneous material, when it becomes method-dependent. However, this problem is an expected feature of a smeared transition in disordered systems and will be discussed in a later section.

Figure 3.15 shows the modified Arrott plots of the sample concentrations, x = 11.4 and 11.6%. This modified Arrott plot now resembles the original Arrott plot with straight, parallel lines. It is now possible to extract the spontaneous magnetization and extrapolate a high field susceptibility (from 0.5 – 5 T) to obtain a modified Curie temperature, T*, and new, modified exponents from the data. The new form of the modified exponents obtained from the susceptibility, χ_H^{-1}, the magnetization, M, and the spontaneous magnetization, M_s, are found as

$$\chi_H^{-1}(T) \sim \left(T - T^*\right)^{\gamma} \tag{59}$$

$$M\left(T^*, H\right) \sim H^{1/\delta} \tag{60}$$

$$M_s(T) \sim \left(T - T^*\right)^{\beta} \tag{61}$$

The exponents found from the modified critical temperature are not consistent with the typical classical critical exponents but are a good description for the data in a wide temperature and field range beyond the classical critical regime. The relationship of these exponents are maintained as

$$\beta\delta = \gamma + \beta \tag{62}$$

From the high field extrapolated susceptibility and the spontaneous magnetization, the value of the exponent is found to be $\gamma = 0.72$ and $\gamma = 0.76$ and the modified critical temperature is a finite and found as $T^* = 10$ K and $T^* = 5.5$ K for $x = 11.4$ and 11.6%, respectively. The notation T^* is used as a reminder that this critical temperature is extrapolated from high fields in a modified Arrott plot.
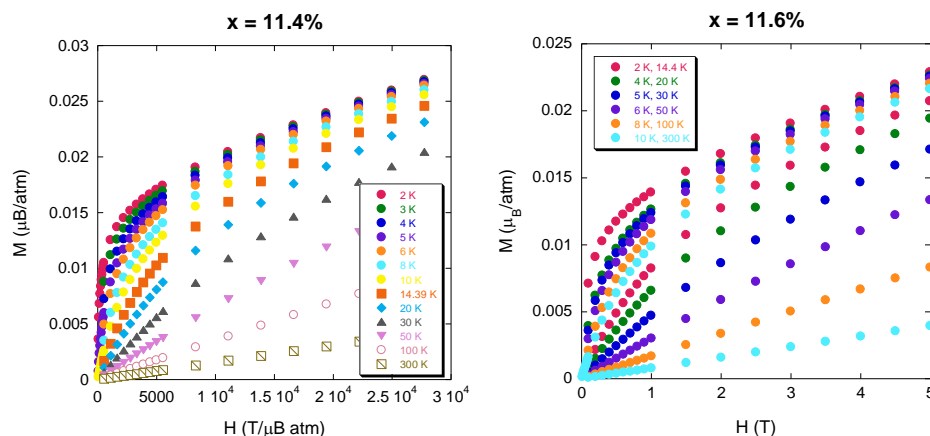
Figure 3.13: a) Magnetization as a function of magnetic field for sample x = 11.4% in the temperature range of 2 - 300 K in fields of 0 - 5 T. b) Magnetization as a function of magnetic field for sample x = 11.6% in the temperature range of 2 - 300 K in fields of 0 - 5 T
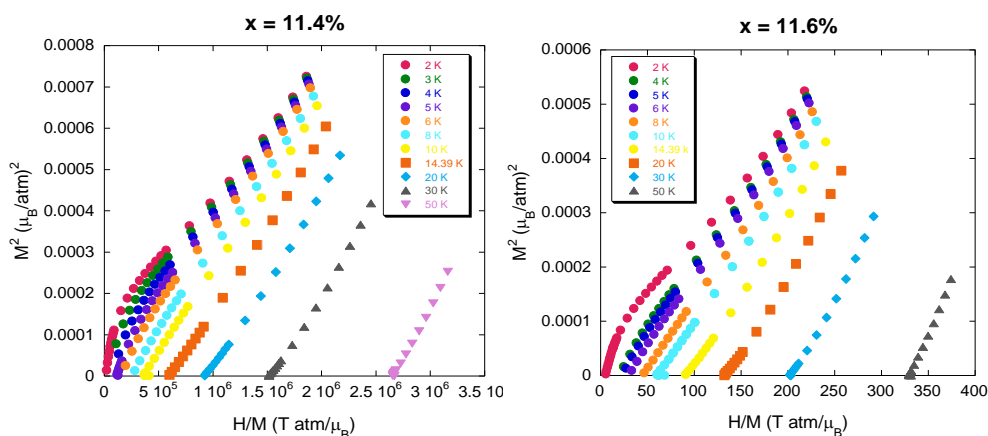
Figure 3.14: a) Arrott plot of sample x = 11.4% b) Arrott plot of sample x = 11.6%
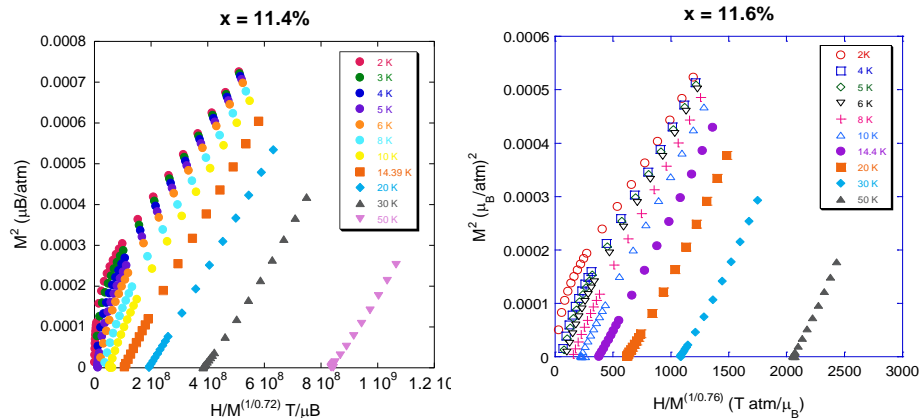
Figure 3.15: a) Modified Arrott plot of vanadium concentration 11.4% with an exponent of $\gamma = 0.72$ and a modified transition temperature of $T^* = 10$ K b) Plot of a modified Arrott plot for x = 11.6% where the exponent $\gamma = 0.76$ and $T^* = 5.5$ K

3.3.4 $Ni_{(1-x)}V_x$ with x > 12%

Figure 3.16 and Figure 3.17 show the magnetization plotted as a function of magnetic field for x = 12.07, 12.25, 13, and 15%, respectively. It is obvious from the plots that these samples with higher vanadium concentration reveal more paramagnetic than ferromagnetic behavior. Figure 3.18 and Figure 3.19 are the corresponding Arrott plots which show curved isotherms and it is not possible to extract any data.

The modified AP description works well for higher vanadium concentrations, x > 11%. Figure 3.20 and Figure 3.21 show the modified AP for samples x = 12.07 − 15% revealing straight, parallel isotherms which allows data to be extracted to obtain an exponent, γ, and a finite critical temperature, T*. For example, the exponents for a representative sample x = 12.25% are β = ½, 1/δ = 0.55, and γ = 0.37 for T* = 2.85 K. Table 3.1 shows the values for the other concentrations. A decrease is seen in the finite modified critical temperature, T*, with increasing vanadium concentration in Figure 3.23 a. The line shows an exponential fit function T* = $(1.27x10^6)*e^{-1.04x}$ with T* < 10 K. T* does not become zero and can not specify a modified critical concentration, x_c* for x ≤ 15%. Figure 3.23 b) shows the extended exponent, γ, from the modified Arrott plot scaling and from χ(T) derived from the Arrott plots, plotted as a function of concentration for all of the samples. For concentrations below 11%, the lines indicate γ ≥ 1. For the concentrations above 11%, γ decreases to 0.03 for x = 15% and an exponential fit describes the data where γ = $\exp^{(-(x-11)/1.3)}$.

These exponents are extremely unusual for phase transitions as disordered systems are expected to show a higher γ. We can use the scaling relation equation to

check how well the exponent, γ, scales with another exponent, $1/\delta$, which we determined separately from M(H). Figure 3.24 a) and b) show magnetization plotted as a function of magnetic field for x = 9.03 − 11% at the critical temperature, T_c, and for x = 11.4 − 15% at the critical temperature T*, respectively. The corresponding fit functions, fit from 1.5 − 5T for x = 9.03 − 11% and from 1 − 5T for x = 11.4 − 15%, follow Equation (59) to extract the exponent, $1/\delta$. One may note the deviations at low magnetic field. Figure 3.25 a) shows the results of this. For x < 11%, the MF value of $1/\delta = 0.33$ is obvious, while for x > 11% $1/\delta$ slowly increases almost up to 1. Figure 3.25 b) compares γ from the modified Arrott plot and the derived γ from the scaling relation (Equation (61)) using $1/\delta$ from M(H) such that $\gamma = (\delta - 1)/2$, for $\beta = \frac{1}{2}$. They are in agreement, within errors, confirming the scaling relation still holds even though these exponents are highly unusual.

An alternative way to show scaling behavior is shown in Figure 3.26. The form of the scaling is $M^2/(T-T^*)$ as a function of $H/M^{(1/\gamma)}/(T-T^*)$ and this is seen for the representative sample x = 12.25% for temperature in the regime of 1.8 K to 18 K and in magnetic fields of 0.5 T to 5 T with keeping $\beta = \frac{1}{2}$.

A good description of the high field magnetization data for x > 11% are power laws with unusual exponents close to a still finite transition and a modified critical temperature, T*, for all concentrations.
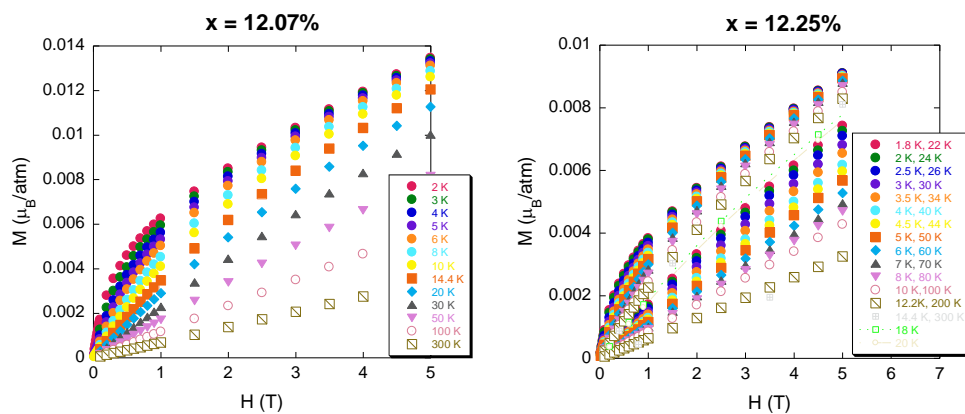
Figure 3.16: a) Magnetization as a function of magnetic field for sample x = 12.07% in the temperature range of 2 K to 300 K b) Magnetization as a function of magnetic field for sample x = 12.25% in the temperature range of 1.8 K to 300 K
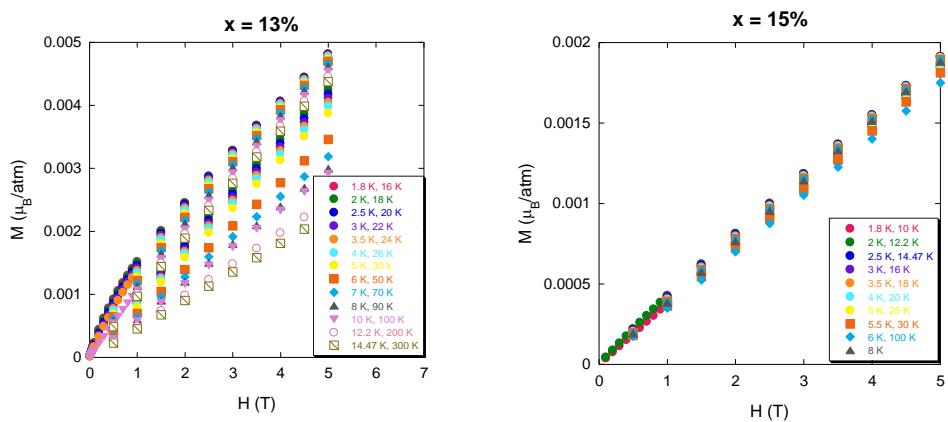
Figure 3.17: a) Magnetization as a function of magnetic field for sample x = 13% in the temperature range of 1.8 K to 300 K, b) Magnetization as a function of magnetic field for sample x = 15% in the temperature range of 1.8 K to 100 K
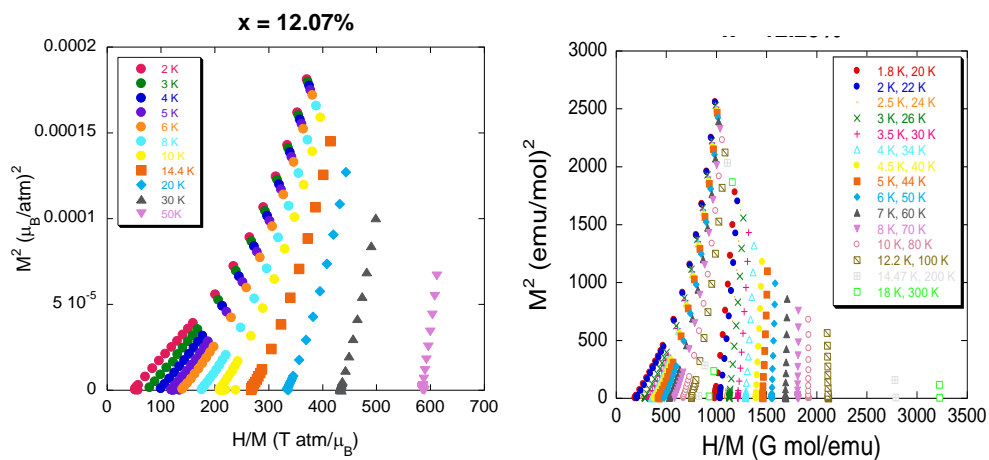
Figure 3.18: a) Arrott plot of sample x = 12.07% b) Arrott plot for sample x = 12.25
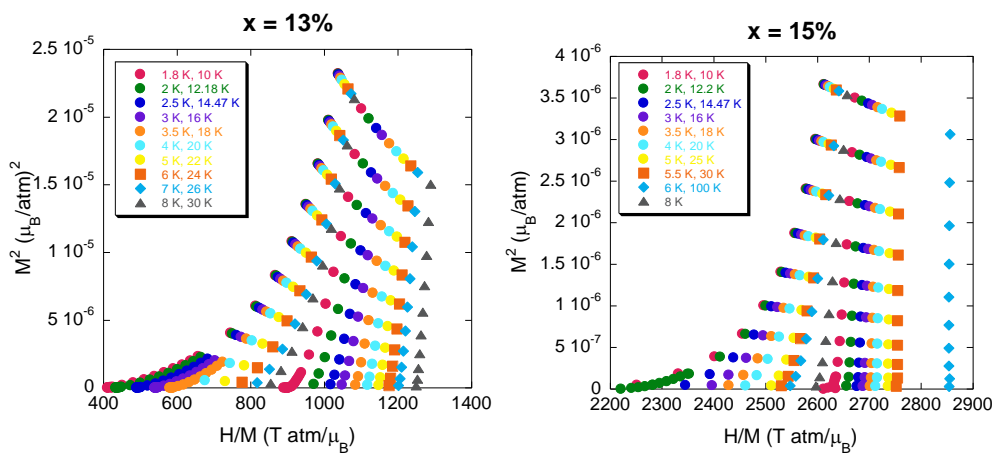
Figure 3.19: a) Arrott plot of sample x = 13% b) Arrott plot for sample x = 15%
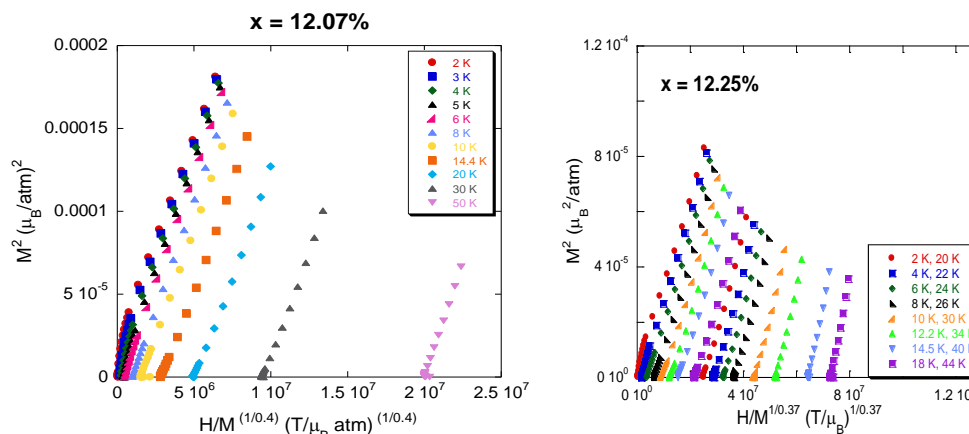
Figure 3.20:a) Modified Arrott plot of vanadium concentration x = 12.07% with an exponent of γ = 0.4 and a modified transition temperature of T* = 5 K showing temperatures from 2 K to 50 K % b) Modified Arrott plot of sample x = 12.25% annealed at 1050 C with exponent γ = 0.37 and a modified Curie temperature of T* = 2.85 K
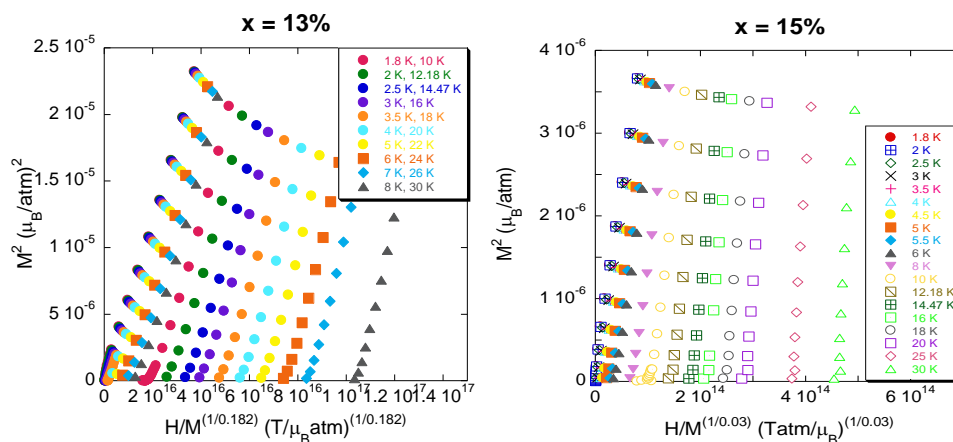
Figure 3.21: a) Modified Arrott plot of vanadium concentration x = 13% with exponent γ = 0.182 and modified transition temperature T* = 2.2 K shown for temperatures from 1.8 K to 30 K, b) Modified Arrott plot of vanadium concentration x = 15% showing exponent γ = 0.03 and a modified transition temperature of T* = 1.13 K in the range of 1.8 K to 10 K

ax (%V)	T_c (K)	T^* (K)	γ	$1/\delta$
9.03	130		1.14	0.3447
10.03	64.5		1.12	0.305
10.71	28		0.97	0.3473
11	15.3		1.05	0.3367
11	14		0.97	0.3348
11.4		10	0.94	0.419
11.6		5.5	0.9	0.371
12.07		5	0.41	0.565
12.25		4	0.36	0.561
12.25		2.85	0.37	
13		2.2	0.182	0.717
15		1.13	0.03	0.932

Table 3.1: Transition temperature, T_c and T^*,and exponents γ, $1/\delta$ for $Ni_{(1-x)}V_x$ from AP and modified AP.
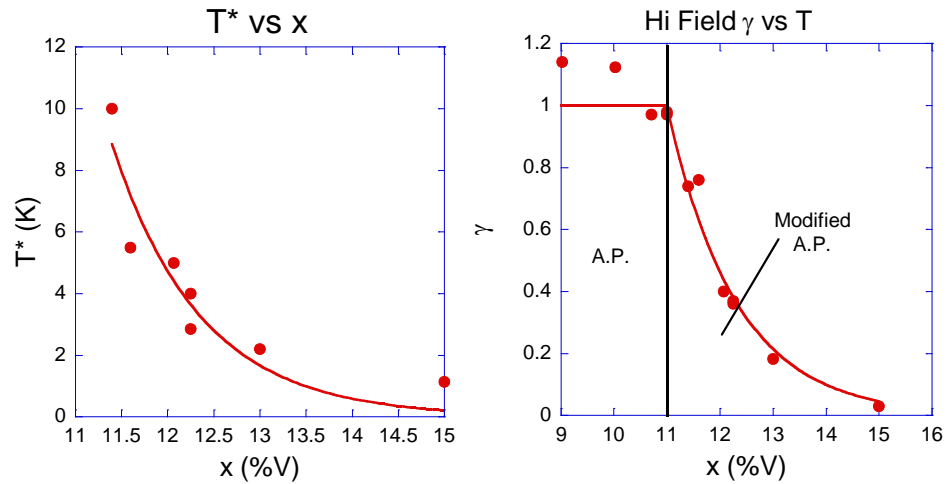
Figure 3.23: a) A plot of the modified critical temperature T^* as a function of vanadium concentration, x, for x > 11% with an exponential fit b) Plot showing the exponent gamma at high field as a function of vanadium concentration, x, as found from the equation $\chi^{-1} \sim (T - T^*)^\gamma$
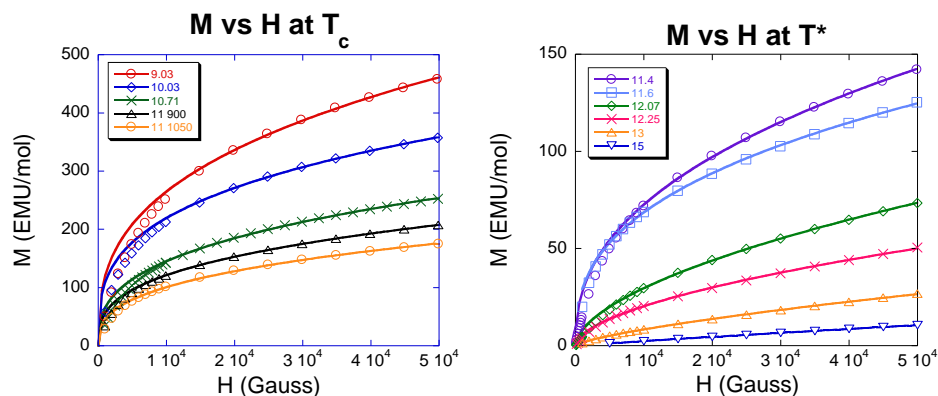
Figure 3.24: a) Magnetization plotted as a function of magnetic field for samples x = 9.03 – 11% at T_c to find the exponent $1/\delta = \alpha$. b) Magnetization plotted as a function of magnetic field for samples x = 11.4 – 15% at T*
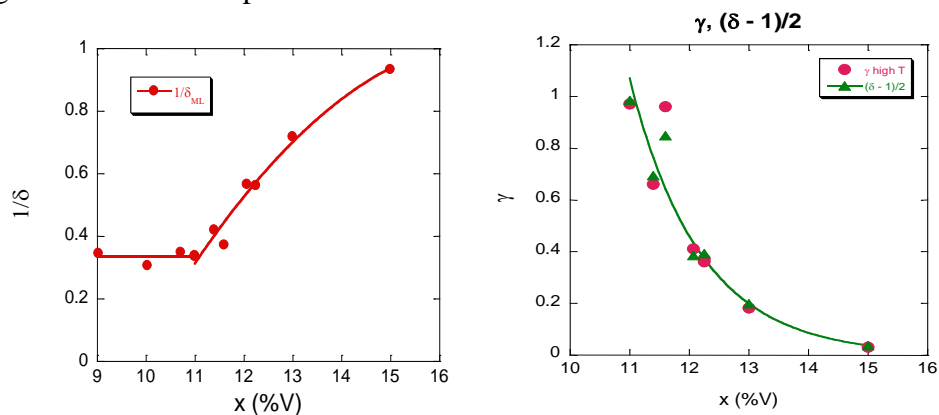
Figure 3.25: a) A plot of the exponent $1/\delta$ as a function of vanadium concentration, x, found from the equation $M(T^*, H) \sim H^{1/\delta}$ b) Graph of the power law exponent γ as a function of concentration. The circles are from the high field extrapolations of the susceptibility and the triangles are from the $1/\delta$ extractions from M(H) data when plotted as $\gamma = (\delta - 1)/2$. The line is a guide to the eye.
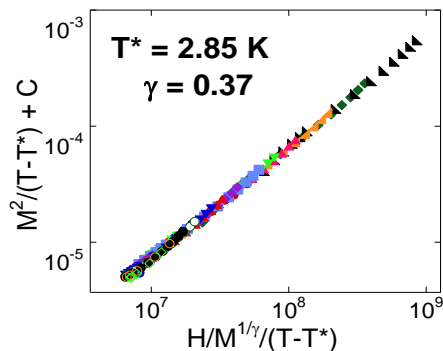
Figure 3.26: Scaling plot for sample x = 12.25% with exponent $\gamma = 0.37$ and modified critical temperature T* = 2.85 K in the regimes of 1.8 -18 K and 0.5 - 5 T
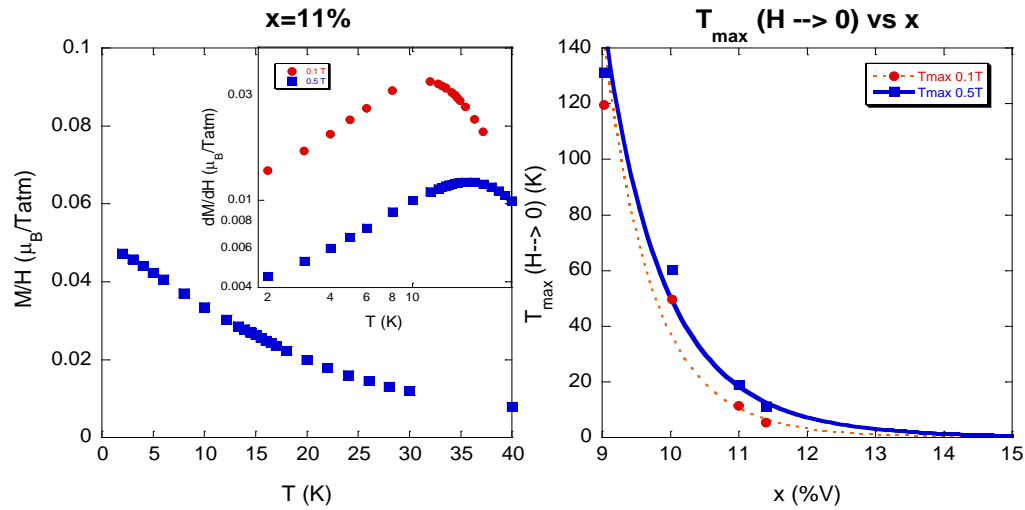
Figure 3.27: a)M/H vs T for x = 11% showing no anomalies at the critical temperature, T_c = 14K. Inset shows dM/dH vs T for magnetic fields of 0.1 and 0.5 T with maxima at a temperature, T_{max}. b) T_{max} plotted as a function of concentration for H = 0.1, 0.5 T with exponential fits.

Previously, the Arrott plots and modified Arrott plots only took into account the high field data because the low field data is normally neglected due to domain orientations and impurities. However, a complete analysis would be to include the low field regime especially since we want to see the effect of disorder. In Figure 3.27 a), M/H is plotted as a function of temperature for, e.g., x = 11% at a magnetic field of 0.5 T and no anomaly is observed at T_c (recall T_c = 14 K), the extrapolated transition temperature from the Arrott plots. However, if the derivative, dM/dH, is taken and plotted as a function of temperature, field dependent maxima are observed at a T_{max}, as seen in the inset of Figure 3.27 a). The maxima at finite H do not correspond to a transition (68); they occur in a simple paramagnet due to Zeeman splitting in the magnetic field.

However, a maximum in $\chi(T)$ when the magnetic field goes to zero indicates a transition. Extrapolating the field dependent T_{max} down to zero magnetic field yields Tmax(0), which is lower than the critical temperatures from the Arrott plots, T_c. This is illustrated in Figure 3.27 b, where the T_{max} corresponds to a maximum at 0.5 T. For the concentrations $x < 12\%$ the T_{max} is a finite value but it goes to zero for the concentrations $x \geq 13\%$.

The determination of the critical temperature is extremely method dependent and is a signature of disorder. The disorder seems to produce an array of T_c values in the sample, called smearing, which change from a power law behavior to an exponential decrease. This is due to different clusters in the material to order individually at different temperatures. This is, e.g., expected in an itinerant Ising system with disorder.

3.4 Magnetic AC Susceptibility Results

Concentrating on the low field behavior, we found maxima in dM/dH(T) at a maximum temperature in a small magnetic field. Simple extrapolations towards $H \rightarrow 0$ resulted in a finite T_{max} which is greater than zero for $x < 12\%$ and a T_{max} approaching zero for $x \geq 13\%$. Around $x = 12\%$ the extrapolations are not clear and the maximum temperature at 0.1 T is less than 2 K, the lowest measurable temperature.

To measure the susceptibility at temperatures lower than 2 K, we used a pick-up coil in a dilution refrigerator. The AC susceptibility, χ_{AC}, could be measured in a very small driving field, $B_{AC} \approx 0.1$ G at different frequencies and dc magnetic fields.
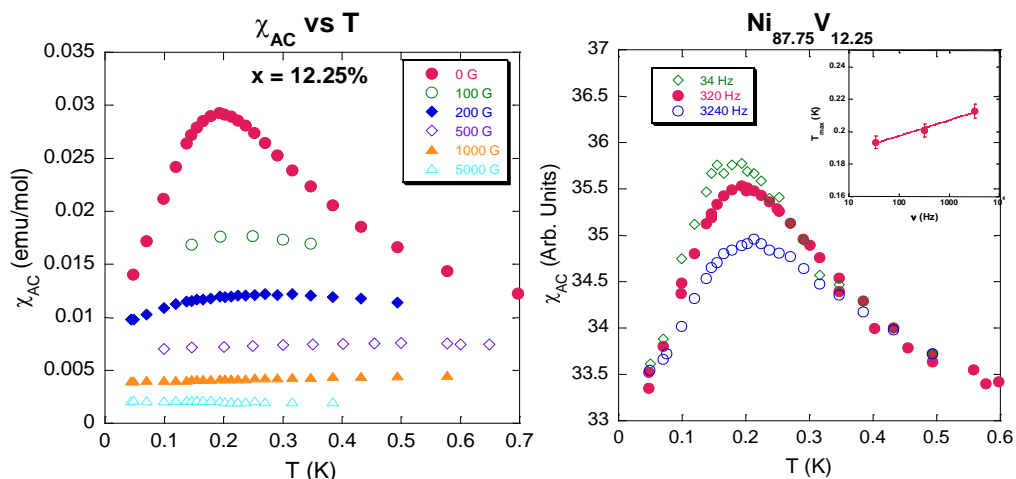
Figure 3.28: a) AC susceptibility as a function of T for x = 12.25% showing a maximum at 0.2 K which is gradually suppressed in a magnetic field, H. The units are calibrated to the SQUID data. b) Frequency dependence of the AC susceptibility for x = 12.25%. Inset shows the maximum temperature, T_{max}, from χ_{AC} as a function of frequency with $dT_{max}/d\log\nu = 0.01$ K/decade ν.

The sample with concentration x = 12.25% was chosen as the ideal candidate for the AC susceptibility tests since: 1) it is in the regime of concentration with power law behavior, x >11%, and 2) it could show a ferromagnetic transition below 2 K. Temperature and field scan measurements were made in a temperature range of 0.05 K – 27 K in magnetic fields up to 8 T. Most of the data was taken with a frequency of 320 Hz of the AC magnetic driving field which was 0.1 Gauss.

Figure 3.28 a) shows the AC susceptibility plotted as a function of temperature in magnetic fields from 0 to 0.5 T with a frequency of 320 Hz. A maximum in the AC susceptibility appears in the data at the maximum temperature, $T_{max} = 0.2$ K, at 0 T and is shifted towards higher temperature and gets suppressed with increasing magnetic field. The frequency dependence of the maximum is shown in Figure 3.28 b) in zero field for frequency $\nu = 34$, 320, and 3240 Hz. T_{max} is shown to increase with increasing frequency

(inset of Figure 3.28) and follows the Vogel-Fulcher law, characteristic behavior of a spin-glass (69).

$$T_{max} = A \log \left(\frac{\nu}{\nu_0} \right) \tag{63}$$

The shift in T_{max} with the frequency is given as $dT_{max}/d\log\nu = 0.01$ K/dec ν which is about what is expected for metallic spin glasses (69). This is the first sign of hysteresis effects in the system. At about 2 K, M(H) data did not show any significant hysteresis, nor was a difference between zero field cooled and field cooled method observed.

T_{max} marks the onset of a cluster glass at very low temperature ≈ 0.2 K, which is roughly 1/3000 of the critical temperature of pure nickel. This temperature is much smaller than the extrapolated critical temperature obtained from the modified Arrott plot, where $T^* \approx 3$ K. Again, this is a sign that different energy and length scales contribute to the magnetic response in this diluted sample, as discussed in Section 3.5.

3.5 Discussion

3.5.1 Clean Weak Itinerant Magnet

In the previous sections, detailed measurements on the resistivity, magnetization, dc susceptibility, and the ac susceptibility were presented to probe the behavior of weak itinerant Ni-V samples. The material showed behavior of a typical weak itinerant ferromagnet (e.g. $\chi^{-1} \sim T_c^{4/3} - T^{4/3}$) for concentrations for $x = 9.03 - 10.71\%$, and mean field behavior for $x = 11\%$, but for concentrations $x > 11\%$ we observed unusual power laws. We extrapolated a finite critical temperature from the modified AP while a

maximum in $\chi_{AC}(T)$ hinted at a cluster glass freezing with T_f at about 1/10 of T* for the same concentration. A critical concentration where $T_c(x)$ vanishes is extrapolated to x_c = 11.2%. However, for $x > x_c$ we see signs of ordering or spin freezing. Obviously we do not deal with a clean FM QCP and have to address scenarios including disorder.

Before this can be done an overview of the typical itinerant properties in terms of a Rhodes-Wohlfarth plot is given. The ratio of the high temperature magnetic moment and the low temperature magnetic moment is considered a sign of "weakness" of the itinerant moment due to increased spin fluctuations. Although Ni-V is an itinerant system and not a system with only local moments, a Curie-Weiss law can be fitted just like in pure nickel over all concentrations (see Figure 3.29) including other fit parameters as discussed later. The CW behavior for Ni-V can be simply understood in an advanced itinerant model. Here we have to allow for additional T-independent term to the Curie-Weiss law to account for the orbital contribution, or band contribution, expected in d-metals called χ_{orb} (68).

$$\chi = \frac{C}{T - \theta} + \chi_{orb} \text{ for T > T}_c,$$ **(64)**

and we can extract an effective high temperature moment, μ_{PM}, from the Curie constant, C, is $C = \mu^2_{PM}/3k_B$. We used this constant as an additional fit parameter which finds $\chi_{orb}{}^o$ ≈ 6e-5 EMU/mol for $x < 11\%$ (see Figure 3.30) which corresponds to the theoretical prediction for Ni (68). For $x > 11\%$, χ_{orb} increases to about 3 times the previously given value. $\chi = M/H$ show a Curie-Weiss law at high temperatures (Figure 3.29) in small magnetic fields (H = 100, 500 G) in the temperature range of $2T_c$ − 300 K. The Curie-

Weiss temperature, θ, for x < 11% is positive showing ferromagnetic coupling and is approximately 10% higher than the critical temperature (Figure 3.31 a). The compounds x > 11% have a negative Curie-Weiss temperature, a response seen with antiferromagnetic coupling or a Kondo coupling. The interaction is approximately zero at x ≈ 12%.

The Curie constant decreases with x as shown in Figure 3.31. The extracted average magnetic moment at high T called the paramagnetic moment, μ_{PM}, as shown in Figure 3.31 b, which can be compared to the ordered moment, μ_s, or the saturation moment, μ_{sat} (Figure 3.32 a), below T_c. The magnetic moment of the ordered moment is observed to be smaller than the saturation moment, μ_{sat}, (extracted at 2 K in a high magnetic field, H = 5 T). Both are significantly smaller than the paramagnetic moment found at high temperatures. The ratio of the paramagnetic moment to the saturation moment plotted as a function of the critical temperature, as seen in Figure 3.32, is consistent with the Rhodes-Wohlfarth plot (36), (22), (38) and is a signature of an itinerant magnet, different than the localized magnets where $\mu_{pm} = \mu_{sat}$. The Rhodes-Wohlfarth criterion (36), (37) states the greater the ratio, μ_{PM} / μ_{sat}, as compared with unity, the magnetic moment is more itinerant. Figure 3.32 b) shows the Rhodes-Wohlfarth plot with the blue squares indicating q_C/q_S, where $q_C = \sqrt{1 + \mu_{PM}^2} - 1$ and $q_S = \mu_{sat}$ as is obtained from the original RW plot to show our data as compared to the theory from Ref. (38).

But the extraction of the paramagnetic moment from the CW law assumes that the moment is uniform throughout the material, which is certainly not the case here for Ni-V. This estimate of μ_{PM} assumes a homogeneous distribution, which is not likely the case for diluted Ni-V. The apparently smaller μ_{sat} compared to μ_{PM} can also occur because of the existence of a few big nickel clusters, N_L. These clusters occur in dilution when the vanadium is randomly distributed causing the nickel to group together. These nickel rich regions in the inhomogeneous distribution have a large moment size μ_L. The different contribution to the saturation magnetization and the Curie constant can provide a rough estimate of the cluster size using the relations below.

$$M_{sat} = N_L \mu_L \cdot f \tag{65}$$

$$C = N_L \mu_L^2 \tag{66}$$

f is the ratio of μ_{PM}/μ_{sat} for pure nickel, $f = 0.6/1.61 = 0.37$. Comparing μ_{sat} and C yields cluster sizes in the range of $8 - 40$ μ_B with cluster concentrations of 0.07% - 11%.

The non ordered regime (x > 11%) showed significant deviations from the typical linear Arrott plots, indicating that ferromagnetism occurs inhomogeneously from the possible presence of large magnetic clusters (60). This has been seen before, where inhomogeneous behavior between the ferromagnetic and paramagnetic transitions in nickel alloys was mentioned in $Ni_xCu_{(1-x)}$ (62) and $Ni_xRh_{(1-x)}$ (70). They showed that the ferromagnetic coupling between giant moments of nickel clusters gave rise to ferromagnetism, and the concentration of clusters increases with increasing nickel content.

The apparent reduction of the magnetic moment in the ordered state is not only due to the itineracy, like in the RW plot, but it is also due to the inhomogeneities that requires a distribution of different sized clusters of magnetic regions containing more nickel than other regions. A better model would be to take into account the magnetic moment from several contributions which is discussed in the next section in a simple cluster model.
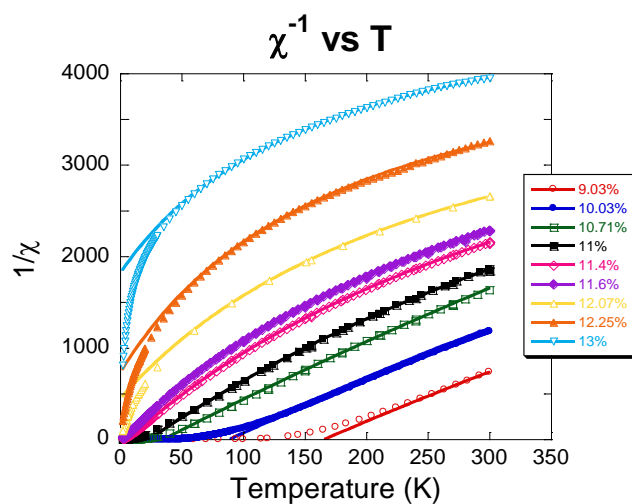
Figure 3.29: Inverse susceptibilities ($1/\chi$ = H/M for a small field of H = 100 G, 500 G) vs T for all x. The lines are fit to Equation (64).
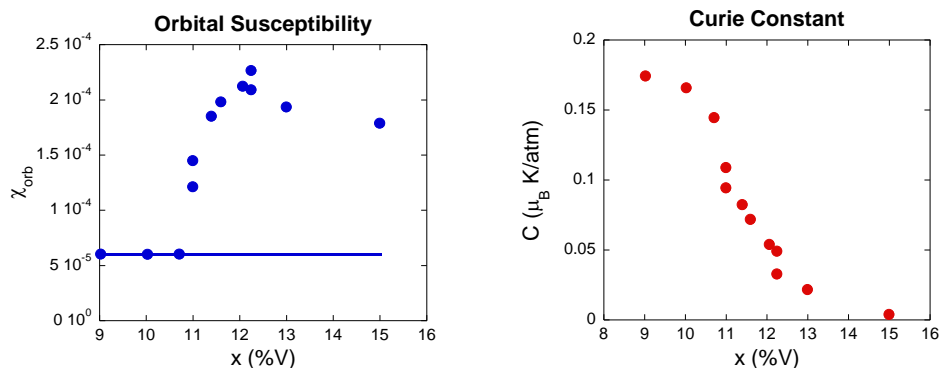
Figure 3.30: a) Temperature independent orbital susceptibility, χ_{orb}, found as an extra term when fitted with the Curie-Weiss law $\chi = \chi_{orb} + C / (T + \theta)$ b) Curie constant, C, as found from $\chi = C / (T + \theta)$ for 500 G data in a temperature range of $2T_c - 300$ K
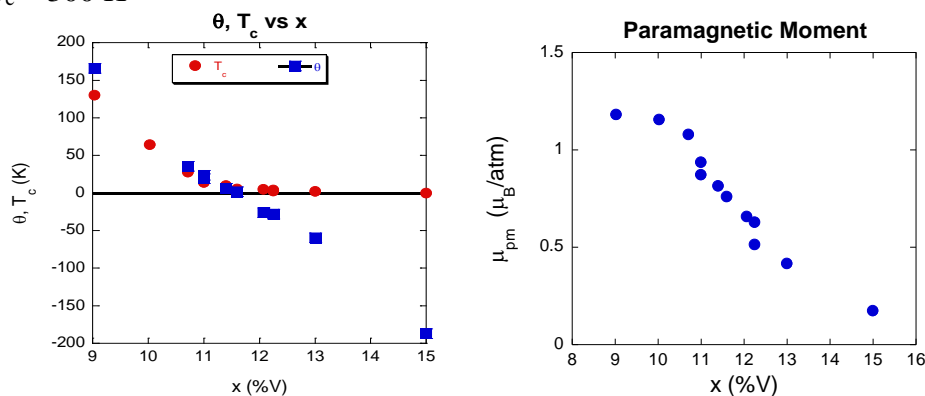
Figure 3.31: a) Curie-Weiss temperature and critical temperature as a function of vanadium concentration b) Paramagnetic moment taken from the Curie-Weiss law $\chi = \mu_{PM}^2 / 3k_B(T + \theta)$ plotted as a function of concentration
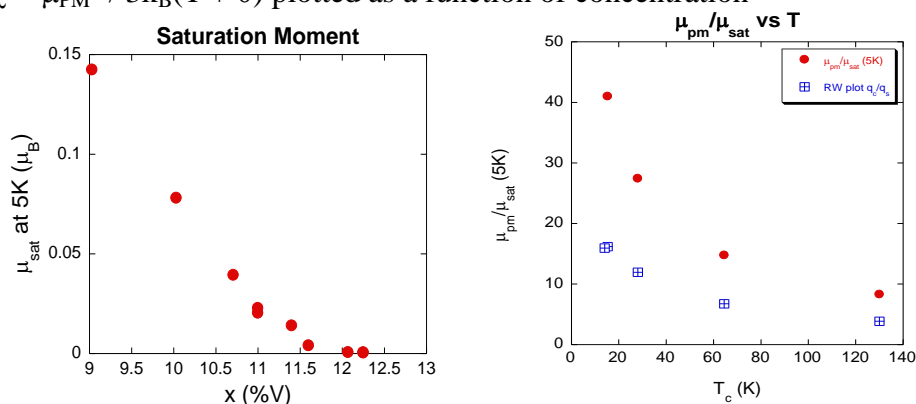
Figure 3.32: a) Saturation moment at 5 K in 5 T as a function of vanadium concentration b) Rhodes-Wohlfarth plot showing a decrease of the ratio of the paramagnetic moment over the saturation moment (μ_{pm}/μ_{sat}) as a function of the critical temperature. The blue squares indicate the ratio qc/qs from **(38)**. See the definition in the text.

3.5.2 Simple Cluster Model

The nickel atoms are thought to form magnetically rich regions due to the dilution of vanadium. In the previous section it is seen that a model of a single cluster size produces a large magnetic moment. The large difference in the ordered moment at high temperature to zero temperature is from the itinerant electrons, but also from the inhomogeneous distribution of magnetic cluster sizes. A different model is now used to probe the behavior (71). Here, it is assumed there are two sizes of moment sizes: there is a small moment size, μ_s, and there are N large clusters with a large moment size, μ_L. Hence, the magnetic moments in the Ni-V samples for $x > 11\%$ can be described by a simple two cluster sizes model which is of the form

$$M(H,T) = N\mu_L \tanh\left(\frac{\mu_L H}{kT}\right) + \frac{\mu_s^2 H}{kT + k\Theta} + \chi_{orb} H \tag{67}$$

N is the amount of large clusters, μ_L is the moment size for the large clusters, μ_s is the moment size for the smaller clusters, $\chi_{orb}H$ is the orbital portion of the magnetic moment and is constant in T, and Θ is the energy scale of the small clusters. The total susceptibility in this model consists of the three contributions from the large, small, and orbital portions, respectively.

$$\chi = \chi_L + \chi_S + \chi_{orb} \tag{68}$$

Here we use,

$$\chi = \frac{M}{H}\bigg|_{H\to 0}, \tag{69}$$

in a small magnetic field of H ≈ 100G. In taking the magnetization equation along with the above equation we obtain the total susceptibility

$$\chi(H,T) \sim \frac{N\mu_L^2}{kT} + \frac{\mu_s^2}{kT + k\Theta} + \chi_{orb} \tag{70}$$

These models were used to fit M(H) for samples with vanadium concentration x = 12.07 − 15%. Figure 3.33 a) shows an M vs. H plot for x = 12.25% with various temperatures from 2 − 100 K in magnetic fields up to 5 T with a fit according to Equation (67). Figure 3.33 b) shows the susceptibility plotted as a function of temperature in a double log plot. The lines show the different contributions of the fit function from Equation (70).

This simple two moment site model fits χ(T) and M(H,T) quite well, see e.g. Figure 3.33 for x = 12.25%. As seen in Figure 3.33 b, the large moment clusters dominate in the low temperature regime, and the small moments dominate in the high temperature regime from about 30 − 300 K. The best fit is a combination of both the small and large moments. Figure 3.34 shows different fit parameters for different concentrations. For samples x = 12.07 - 15% the small average moment has a moment size of 0.3 μ_B/Ni or less, and the large moment cluster has a moment size of 10 μ_B/Ni or less. Both moment sizes decrease as vanadium content is increased, due to the decreased amount of nickel in the sample. Both the number of clusters, N, and the large moment size, μ_L, diverge towards x_∞ = 11.4% following a power law decreasing with the vanadium concentration as seen in Figure 3.34, which is close to the extrapolated critical concentration where T_c

vanishes, $x_c = 11.2\%$. Above, x_c, there is evidence for "independent" clusters with sizes of several Bohr magnetons.

The small moments have a large energy scale (Figure 3.35), $\left|\Theta\right| \approx 40 - 90$ K, meaning they have a strong coupling due to either the interactions between each other or due to the conduction electrons. On the contrary, the large clusters have an energy scale that is very small, $\Theta \approx 0$, meaning that the clusters have either weak or no fluctuations and that they are more independent to one another.

We did not have any measurements to directly address the spin fluctuation dynamics. However, from this simple two moment model describing the bulk susceptibility data, we can already deduce an interesting relationship between the cluster sizes and their fluctuations which becomes important in the Griffiths phase scenario as seen in the next section. This fluctuation rate, $\left|\Theta\right|$, increased when the moment size decreased meaning that the small moments fluctuate faster than the big clusters contributing less to χ at low T. Then the large clusters, which fluctuate very slowly, dominate the low temperature behavior.
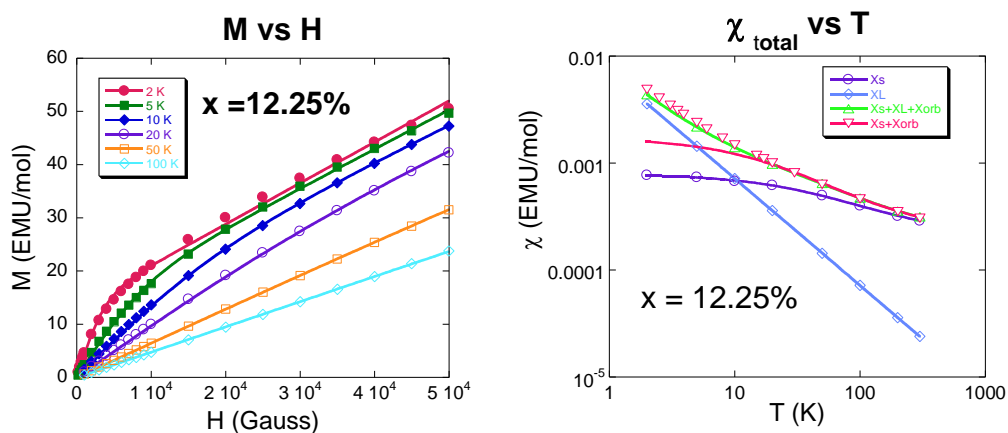
Figure 3.33: Magnetization vs magnetic field a) for x = 12.25% and χ = M/H vs T b). The triangles in b) show the two cluster size model, and the others show different contributions.
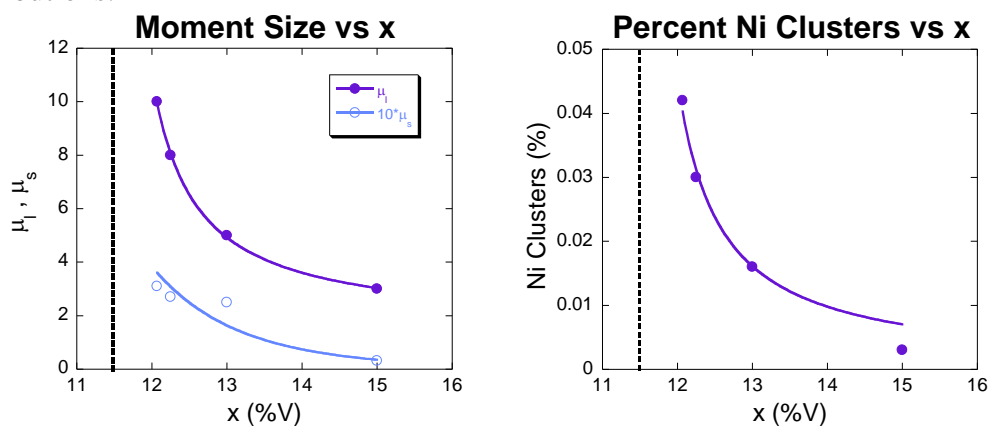
Figure 3.34: a) The size of the large cluster moment, μ_L, and the small cluster moment, μ_s, plotted as a function of vanadium concentration b) The percentage of nickel clusters as a function of vanadium concentration
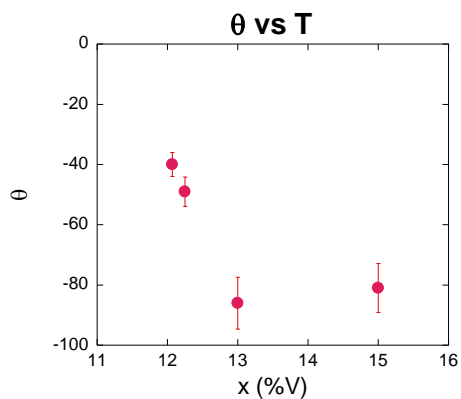
Figure 3.35 : Curie temperature as extracted from the Curie-Weiss law fit from 2Tc – 300 K for x = 12.07 – 15%

3.5.3 Griffiths Phase Scenario

In the previous sections, it was seen that Ni-V is a weak itinerant disordered ferromagnet. NFL behavior has been observed in the resistivity and susceptibility. Upon probing the regime for $x > x_c$, an exponential decrease is seen in estimates of the critical temperature signaling a smeared phase transition, and spin glass freezing maxima in the low temperature regime were observed. Magnetic clusters have been seen using a simple model of small and large moment sizes, where the larger moments dominate at low temperature. It is possible that the NFL behavior observed is due to the critical fluctuations of a quantum Griffiths phase (72). Our material is a possible scenario for a Griffiths phase, which is when large, rare clusters (see Figure 3.36) dominate the low temperature behavior in a complex system near a ferromagnetic quantum critical point and the signatures are simple power laws.

These effects should be seen in disordered systems for 3-d Heisenberg and for Ising systems (55). Not very many materials are investigated in the perspective of a Griffiths phase close to a ferromagnetic quantum phase transition even though other ferromagnetic transition metal alloys like Ni-Cu (29) (62) show magnetic clustering when diluted. It has been predicted to exist in Ni-Pd (73) even though it has not yet been seen experimentally. It is being investigated for Ni-V in this present dissertation.

According to the expectations for a magnetic Griffiths phase as introduced in Chapter 1, the low field susceptibility χ_0^{-1} should portray a power law with exponent (1 −
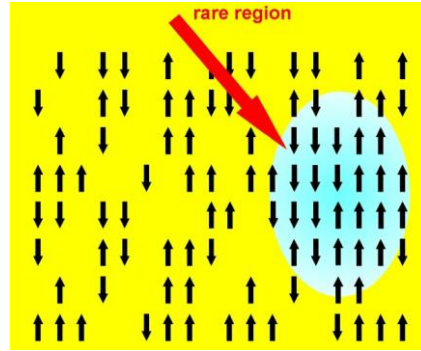
Figure 3.36 Schematic diagram showing a rare region amid an unordered material **(83)**

α), where the non-universal exponent α should be the same value as the high field exponent, α_H, obtained from the magnetization plots as a function of field, M(H).

$$\chi_0 \sim \frac{C}{T} \sim \frac{1}{T^{1-\alpha}}$$

(71)

$$M(H) \sim H^{\alpha_H} \quad \text{for high field H} > \Theta$$

(72)

A signature of the Griffiths phase is that the power law for the susceptibility is less than 1(see ref. of (74)).

Figure 3.37 shows the low field χ vs. T and the low temperature M vs. H in a log-log plot for x > 11%, subtracting out a small χ_{orb} contribution. At low temperatures the Ni-V samples indeed follow a power law in the low field susceptibility in χ_0^{-1} as seen in Figure 3.37 a). In the same plot, a power law fit of the high temperature regime is made and the power γ is obviously smaller than the low temperature fit. Even though the power γ_L is larger than γ_H obtained from the high field susceptibility, it is observed to still be less than 1 for all x > 11% as seen in Figure 3.38. In the same plot of the critical exponents, it is seen that the high temperature exponent of the susceptibility matches the low temperature exponent of the magnetization as $\gamma_H = 1 - \alpha_H$. Since Ni-V shows these

particular signatures when probed in the critical regime, a Griffiths' phase is imminent but in what regime? From Figure 3.38, the critical exponent, γ_L, does not agree very well with $1 - \alpha_H$ indicating a Griffiths' phase is present for a wide temperature region, from 300 K down to 10 K. Below 10 K, a deviation occurs.
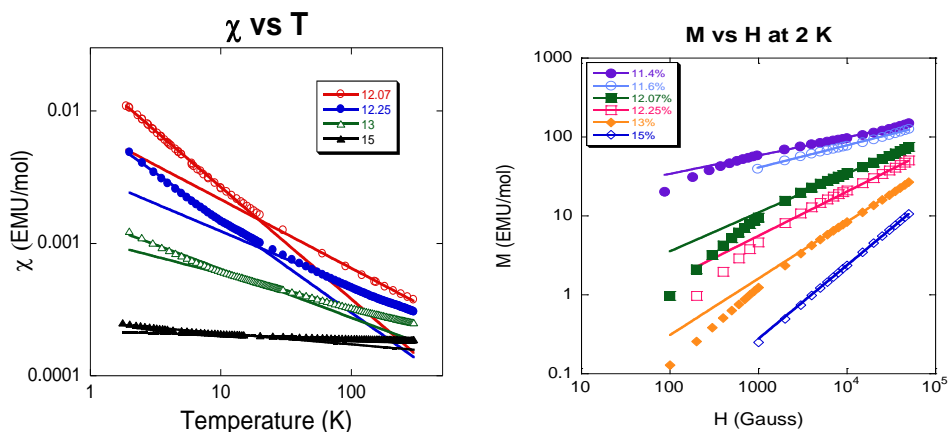
Figure 3.37: a) Low field susceptibility plotted as a function of temperature for samples x = 12.07 – 15% in a log-log plot subtracting out an orbital susceptibility of χ_{orb} = 6e-5 emu/mol from the demagnetized data. A low temperature fit displaying a different gamma exponent compared with high temperature is seen and is shown in the next figure. b) Double log plot of Magnetization vs magnetic field at 2 K for x > 11% to show the critical exponent α.
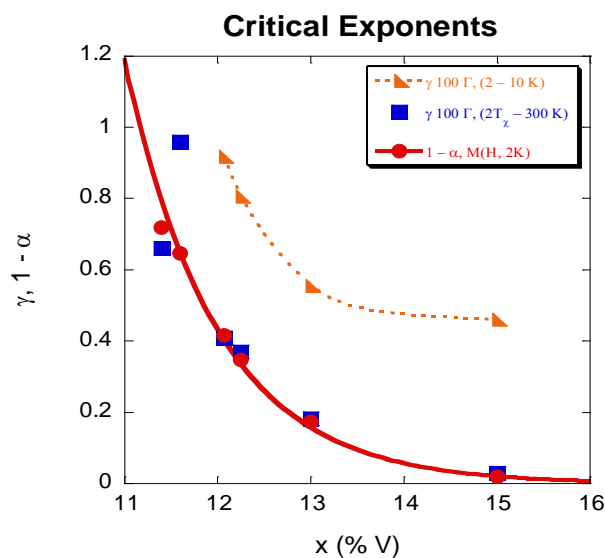
Figure 3.38: Critical exponents γ, 1-α vs vanadium concentration as extracted from χ vs T in both the low and high temperature regimes, and from M vs H at 2 K.

At this point, one may ask why the system portrays a quantum Griffiths phase and the answer relies on the dimensionality of the clusters as explained in Chapter 1. If the effective dimensionality of a cluster is less than the lower critical dimension, d_c^-, then the system does not order. For a disordered itinerant Heisenberg magnet, the dynamical exponent, due to conduction electron damping with $z = 2$, is equal to the effective dimension of the rare region which is directly at the lower critical dimension, $d_{eff} = z = d_c^- = 2$ (55). A quantum critical point of infinite randomness exists and controls the Griffiths phase, which shows power law behavior (24). A more detailed analysis of the Heisenberg system yields power laws with logarithm corrections. Including the log terms does not change the power law description significantly, and they cannot explain the increase of γ towards low T. This is in the region from 10 K and up to possibly 627 K, the critical temperature of pure nickel.

At lower temperatures, it might be possible that dissipation effects occur due to the conduction electrons through long range RKKY interactions between the clusters (56), (19). This dissipation causes $z > 2$ (24) resulting in the effective dimension to be larger than the lower critical dimension. The large clusters will independently stop fluctuating, leading to magnetic domain freezing, and this permits each individual cluster to have its own "critical temperature", resulting in a smeared critical temperature for the bulk system. (19), (55). The cluster fluctuations cease to exist close to a quantum critical point, destroying the Griffiths phase. At this point the clusters are all frozen, contributing to a magnetic response that follows a Curie law, $\chi(T) \sim 1/T$, called superparamagnetism. The freezing of the clusters is mentioned to exist close to a quantum percolation threshold

(24). Immediately after some of the clusters freeze, they order into a cluster glass phase at some very low finite temperature. This has been suggested to be a basic occurrence in disordered itinerant systems where $d_{eff} > d_c^-$ (56). The increased γ_L towards low T in χ can be modeled by an extra 1/T contribution to χ of the already frozen clusters.

The phase diagram of Ni-V in Figure 3.39 shows the logarithm of the temperature plotted as a function of vanadium concentration where the critical temperature is obtained for various regimes. The transition between the ordered ferromagnetic state and the critical regime shows a smeared transition temperature for x = 11.4 - 15% with a Griffiths phase in the range from 10 K to 300 K. Below the smeared transition, superparamagnetism is observed. A cluster glass phase is detected at very low temperatures, e.g. at T_g = 0.2 K for x = 12.25%. Further investigation into the other concentrations at low temperatures will most likely show a cluster glass phase, but that is yet to be seen.

In conclusion, the alloy Ni-V is a weak disordered itinerant ferromagnet that portrays 3-d Heisenberg symmetry. It is a typical itinerant ferromagnet up to 11%, and it shows NFL behavior for higher vanadium concentrations. A quantum Griffiths phase is observed from 300 K – 10 K. At lower T, a smeared phase transition leads to a cluster glass phase at very low temperatures. This scenario is expected for a 3-d disordered itinerant Heisenberg system with long range RKKY interactions.
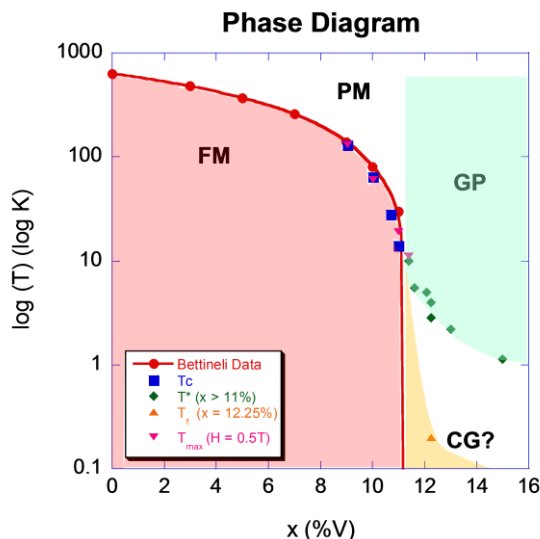
Figure 3.39: Phase diagram of Ni-V showing a Griffiths phase in a ferromagnetic itinerant Heisenberg system. Deviations occur towards lower T due to RKKY interactions giving rise to cluster glass phase

Ni-V seems to be a model system to show all the signatures of a new QCP introduced by disorder. Many other binary Ni alloys have been investigated but they have not been reported to show a Griffiths' phase. For example, Ni-Pd shows all the signatures of a clean QCP. Why is disorder present and relevant in Ni-V but not in Ni-Pd? Our results show that alloying vanadium distorts the magnetic nickel much more than palladium, which is in the same group as nickel in the periodic chart. The most obvious sign is that the critical concentration of vanadium is much smaller than the critical concentration of palladium. Vanadium has five less electrons than nickel and not only does it change the electronic concentration, it creates a local defect in the alloy. The moment at the vanadium site is expected to be small, but vanadium reduces the nickel moment of the close nickel neighbors (75) (76). This leads to a reduced moment region with radius, r_{eff}, which is proportional to the lattice constant, a, and is on the order of two

nickel shells. This results in an inhomogeneous magnetic moment density. That x_c is much smaller than the percolation threshold of $p_c = 80\%$ for an fcc site percolation supports the idea that vanadium changes the moment in a larger regime than just the local vanadium atom. This makes Ni-V an ideal system to study a disordered quantum critical point.

Chapter 4

Summary

Resistivity and magnetization measurements were performed in a wide temperature and magnetic field regime for the weak itinerant disordered ferromagnetic alloy $Ni_{(1-x)}V_x$. The critical temperature, T_c, vanishes rather quickly with increasing vanadium concentration towards a critical concentration of only $x_c = 11.2\%$ compared with, e.g., $Ni_{(1-x)}Cu_x$ with $x_c = 56\%$ (62), or even $Ni_{(1-x)}Pd_x$ with $x_c = 97.5\%$ (61). By being able to control the critical temperature in these alloys with x, it is possible to probe predictions for a zero temperature quantum critical point for a 3d itinerant ferromagnet including disorder.

Already from the temperature dependent resistivity, $\rho(T)$, measurements, we see signs of unconventional behavior in Ni-V different than in normal metals but also different than a clean ferromagnetic quantum critical point. Power laws in the resistivity are observed with exponents of $n < 2$ in a wide concentration regime which is a sign of non-Fermi liquid behavior. However, it is expected that $n = 5/3$ for a clean ferromagnetic quantum critical point at the critical concentration where the critical temperature goes to zero. Instead, n reaches lower values towards the critical concentration and does not quickly recover to 2 with higher concentration. Furthermore, the high residual resistivity,

$\rho(T \rightarrow 0)$, indicates that inhomogeneities are present in Ni-V that affect the nature of the non-Fermi liquid behavior and the quantum critical point.

Magnetization measurements allow a good description of this weak itinerant ferromagnet with low or vanishing T_c. Two different regions are distinguished: $x < 11\%$ and $x > 11\%$. The magnetization for $x < 11\%$ follows expectations for clean weak itinerant magnets. The Arrott plots show straight, parallel lines, and the spontaneous magnetization and the magnetic susceptibility show a $T^{4/3}$ dependence close to the critical concentration. The extrapolated critical temperature, $T_c(x)$, decreases as a power law towards the critical concentration, $x_c = 11.2\%$ as does the spontaneous magnetization. At high temperatures, the paramagnetic moment decreases and the ratio of the paramagnetic moment to the spontaneous moment also decreases, indicating spin fluctuations in the material. All these indications point toward an itinerant ferromagnetic quantum critical point, where quantum fluctuations finally destroy the long range ferromagnetic ordered state.

For $x = 11\%$, the material still shows linear isotherms in the Arrott plots. However, it does not show the $T^{4/3}$ dependence indicating that there is already enough disorder to alter the behavior from a clean weak itinerant ferromagnet. This description completely breaks down for $x > 11\%$. The Arrott plots are now curved and a modification of the Arrott plots include new critical exponents that differ from mean field theory or typical exponents expected for a 3-d ferromagnet. The magnetic susceptibility and the spontaneous magnetization as extracted from the modified Arrott plots show power laws for a wide temperature and magnetic field regime and satisfy scaling relations for

classical phase transitions close to the critical temperature, but with modified exponents. A modified critical temperature, T*, is extracted and not only does it decrease with concentration as an exponential, the determination of the critical temperature is model dependent. High field extrapolations of the modified Arrott plots lead to $T_c \approx 2$ K, whereas, low field signatures in dM/dH leads to a different ordering temperature of 0.2 K. Even with high dilution, for x →15%, no simple paramagnetic phase is recovered.

We can construct a phase diagram including the critical temperature, T_c, from the Arrott plots and the modified critical temperature, T*, from the modified Arrott plots. While $T_c(x)$ initially follows a power law as expected towards a clean quantum critical point, T*(x) is decreasing exponentially which can be induced by the presence of disorder. Furthermore, T*(x) does not vanish indicating it is not possible to determine a critical concentration, x_c. When the different critical temperatures are not sharply defined, there is a smear in the phase transition, also known as smearing (19).

In probing the size of the moments in Ni-V, models with single uniform sized moments cannot describe the data. Instead, a simple model of at least two moment size distributions is applied by assuming all moments is either small or large. The results showed a few large clusters dominate the magnetic susceptibility, χ, at low temperatures and many small moments that dominate χ at high temperatures. The interaction of the small moments due to the conduction electrons, as fitted by a Curie-Weiss temperature, is large and negative as for antiferromagnetic coupling. The interaction of the large clusters is fitted as zero. This particular model fits the data well, indicating that different moment sizes and different fluctuation rates occur in Ni-V.

Although this all looks complicated, the best description is simple power laws in $\chi(T)$ and $\chi(H)$ with unusual exponents. These are all signs that disorder modifies the quantum critical scenario. Recent theoretical models predict two distinct cases for itinerant ferromagnets. For Ising spins, large rare magnetic regions can order individually leading to a cluster glass phase at low temperature. On the other hand, a new infinite-randomness quantum critical point is expected for Heisenberg spins with a quantum Griffiths' phase in the disordered regime characterized by non-universal exponents. Clear evidence of a quantum Griffith' phase is seen in an extended temperature regime down to 10 K, in accordance with Heisenberg spin symmetry. However, we also see signs of a smeared critical temperature and a cluster glass phase at very low temperature. Since both cases are critically dependent on the damping effect of the conduction electrons, we assume that Ni-V represents a Heisenberg spin showing a quantum Griffiths' phase, but an additional coupling mechanism of RKKY becomes apparent at low temperature. This changes the damping of the conduction electrons to become more damped to allow a cluster glass in this Heisenberg system. Theoretical predictions support this scenario.

In conclusion, a possible cause of NFL behavior in a disordered itinerant ferromagnetic Heisenberg magnet is an infinite-randomness quantum critical point with a quantum Griffiths phase. The subject material for this dissertation, Ni-V, is one of the very first itinerant ferromagnetic compounds to experimentally exhibit a quantum Griffiths' phase with a wide range of exponents. This is an exciting revelation in

condensed matter physics as the search for unconventional phases in quantum critical regimes is continuously ongoing and demanding.

In the following, I mention a future direction to further establish the characteristics of a disordered quantum critical point. The next step to characterize the Griffiths' phase demands a microscopic view of cluster sizes and cluster spin dynamics which could be made through the use of neutron scattering techniques. An initial attempt at this was done for Ni^{58} isotope diluted with x = 11.11 and 12.25% vanadium conducted with small angle neutron scattering (SANS) techniques in temperatures from 2 – 300 K in fields up to 5 T at NIST in Gaithersburg, MD. The results were not included in this dissertation since a detailed analysis was not possible at this stage. But preliminary results for x = 11% show increasing correlation lengths towards lower temperatures which were strongly field dependent, while the signal for x = 12.25% was too small to be resolved from the intense non-magnetic background due to the incoherence of vanadium and the chemical distribution. To get a clearer picture of the magnetic cluster distribution and dynamics, other compounds with elements with less incoherent scattering should be investigated in the framework of a Griffiths' phase and studied with SANS and inelastic neutron scattering techniques (e.g. triple axis spectrometer or spin echo spectrometer.)

Another possibility for future experiments is to determine if NFL behavior exists in a disorder induced heavy fermion ferromagnet, of which only a few have been observed (6). Samples of the compound CeAuGe have been created, annealed, and measured in the SQUID magnetometer to reveal a transition temperature of $T_c = 11$ K.

Diluted samples with La, Cu, or Si have been made to try to suppress the critical temperature and create magnetic disorder in the material, just like in Ni-V. But since these samples are more anisotropic than Ni-V, the Arrott plot analysis does not work in the polycrystalline samples.

Also, since the magnetization results showed dependence in the annealing method of the samples, further studies are needed to examine our annealing techniques to determine the best possible process for our samples to produce a "perfectly random" distribution of non-magnetic sites and excluding chemical clustering. This could potentially decide if the smearing of the phase transition and the observed cluster glass phase are due to intrinsic RKKY interactions, or a result of an increased weight of the larger clusters due to chemical clustering.

As I end the last chapter of this dissertation, I would hope that these experiments would be continued by the next generation of graduate students and for them to learn from and enjoy doing these experiments as much as I have.

Bibliography

1. **Mohn, P.** *Magnetism in the Solid State.* Berlin : Springer, 2003.

2. **Lohneysen, H., Rosch, A., Vojta, M., and Wolfle, P.** 2007, Rev. Mod. Phys. , Vol. 79, p. 1015.

3. **Sachdev, S.** *Quantum Phase Transitions.* s.l. : Cambridge, 1999.

4. **Schofield, A.J.** 2, 1999, Contemporary Physics, Vol. 40, pp. 95-115.

5. **Sondhi, S.L., Girvin, S.M., Carini, J.P., and Shahar, D.** 1, 1997, Rev. of Mod. Phys., Vol. 69, p. 315.

6. **Stewart, G.R.** 2001, Rev. Mod. Phys., Vol. 73, p. 797.

7. **Millis, A.J.** 10, 1993-II, Phys. Rev. B, Vol. 48, p. 7183.

8. **Seaman, C.L., et al.** 1991, Physical Review Letters, Vol. 67, p. 2882.

9. **Maple, M.B. et al.** 1994, J. Low Temp. Phys., Vol. 95, p. 225.

10. **Julian, S.R. et al.** 1996, J. Phys. Cond. Matt., Vol. 8, pp. 9675-9688.

11. **Bauer, E.B. et al.** 2005, Phys. Rev. Lett., Vol. 94, p. 046401.

12. **Lenkewitz, M., et al.** 1997, Phys. Rev. B, Vol. 55, p. 6409.

13. **Kato, M. et al.** 2000, J. Phys.: Condens. Matter, Vol. 12, pp. 1769-1779.

14. **Okpalugo, D.E.** 1985, J. Phys. F: Met. Phys., Vol. 15, pp. 681-692.

15. **Hong, C.** 2001, Phys. Rev. B, Vol. 63, p. 092504.

16. **Kim, D.** 2003, Phys. Rev. B, Vol. 67, p. 100406(R).

17. **Pfleiderer, C., McMullan, G.J., Julian, S.R., and Lonzarich, G.G.** 1997, Phys. Rev. B, Vol. 55, pp. 8330-8338.

18. **Pfleiderer, C. et. al.** 2004, Nature, Vol. 427, p. 227.

19. **Vojta, T.** 2006, J. Phys. A: Math. Gen., Vol. 39, pp. R143-R205.

20. **Nicklas, M. et al.** 21, 1999, Phys. Rev. Lett., Vol. 82, p. 4268.

21. **Lonzarich, G.G.** *The Electron.* [ed.] M. Springford. Cambridge/New York : Cambridge University Press, 1997.

22. **Moriya, T.** *Spin Fluctuations in Itinerant-Electron Magnetism.* Berlin : Springer, 1985.

23. **Houghton, R.W.** 4, 1970, Phys. Rev. Lett., Vol. 25, p. 238.

24. **Vojta, T., Kotabage, C., and Hoyos, J.** 2009, Phys. Rev. B, Vol. 79, p. 024401.

25. **Amamou, A., et al.** 1975, J. Phys. F: Met Phys., Vol. 5, pp. 1342-1358 .

26. **Acker, F., et al.** 5, 1976, J. Phys. F: Metal Phys., Vol. 6.

27. **Bettinelli, D. et al.** 09-10, 1999, Int. J. Mod. Phys. B, Vol. 13, pp. 1169-1175.

28. **Amamou, A. et al.** 1974, Journal de Physique, Vol. 35, pp. C4-217.

29. **Hicks, T.J., el al.** 11, 1969, Phys. Rev. Lett., Vol. 22, p. 531.

30. **Aldred, A.T. et al.** 16, 1970, Phys. Rev. Lett., Vol. 24, p. 897.

31. **Kittel, C.** *Introduction to Solid State Physics.* 7th. Singapore, New York : John Wiley & Sons, Inc., 2000.

32. **Aharoni, A.** *Introduction to Theory of Ferromagnetism.* s.l. : Oxford University Press, 2000.

33. **Weiss, P.** 1907, J. Phys. Radium, Vol. 6, p. 661.

34. **Heisenberg, W.** 1928, Z. Phys., Vol. 49, p. 619.

35. **Stoner, E.C.** 1938, Proc. R. Soc. London Sect. A, Vol. 165, p. 372.

36. **Wohlfarth, E.P.** 1978, J. Magn. Magn. Mater., Vol. 7, p. 113.

37. **Moriya, T.** 1983, J. Magn. Magn. Mater., Vol. 10, pp. 31-34.

38. **Takahashi, Y.** 2001, J. Phys.: Condens. Matter, Vol. 13, pp. 6323-6358.

39. **Ogawa, S, et al.** 5, 1967, J. Phys. Soc. Japan, Vol. 22, p. 1214.

40. **Sigfusson, T., et al.** 1982, Phys. Scr., Vol. 25, p. 720.

41. **Arrott, A.** 6, 1957, Phys. Rev., Vol. 108, p. 1394.

42. **Domb, C. and Green, M.** *Phase Transitions and Critical Phenomena.* s.l. : Academic Press, 1976. Vol. 5a.

43. **Collins, M.** *Magnetic Critical Scattering.* s.l. : Oxford University Press, 1989.

44. **Baierlein, R.** *Thermal Physics.* Cambridge : Cambridge University Press, 1999.

45. **Hertz, J.A.** 1976, Phys. Rev. B, Vol. 14, p. 1165.

46. **Arrott, A. and Noakes, J.** 1967, Phys. Rev. Lett., Vol. 19, pp. 786-789.

47. **Perumal, A. and Srinivas, J.** 2003, Phys. Rev. B, Vol. 67, p. 094418.

48. **Landau, L.D.** 1957a, Sov. Phys. JETP, Vol. 3, p. 920.

49. **Landau, L.D.** 1957b, Sov. Phys. JETP, Vol. 5, p. 101.

50. **Harris, A.B.** 1974, J. Phys. C, Vol. 7, p. 1671.

51. **Vojta, T., and Schmalian, J.** 2005, Phys. Rev. Lett., Vol. 95, p. 237206.

52. **Griffiths, R.B.** 1969, J. Math. Phys., Vol. 10, p. 1559.

53. **Castro Neto, A.H. and Jones, B.A.** 2004, arXiv:cond-mat/0411197v1.

54. **Millis, A.J., Morr, D.K., and Schmalian, J.** 2004, arXiv:cond-mat/0411738v1.

55. **Vojta, T. and Schmalian, J.** 2005, Phys. Rev. B, Vol. 72, p. 045438.

56. **Dobrosavljevic, V. and Miranda, E.** 2005, Phys. Rev. Lett., Vol. 94, p. 187203.

57. **Blundell, S.** *Magnetism in Condensed Matter.* New York : Oxford University Press, 2001.

58. http://www.mrl.ucsb.edu/mrl/centralfacilities/chemistry/fundmanual.pdf. [Online] Quantum Design.

59. **Weiss, P. and Forrer, R.** 1926, Ann. Phys. (Paris), Vol. 5, p. 153.

60. **Amamou, A. and Loegel, B.** 1973, J. Phys. F: Metal Phys., Vol. 3, p. L79.

61. **Nicklas, M. et al.** 21, 1999, Phys. Rev. Lett., Vol. 82.

62. **Kouvel, J.S. and Comly, J.B.** 11, 1970, Phys. Rev. Lett., Vol. 24, pp. 598-601.

63. **Smith, J.F., Carlson, O.N. and Nash, P.G.** 3, 1982, Bull. Alloy Phase Diagrams, Vol. 3, pp. 342–348.

64. **Moreen, H.A., et al.** 1971, J. Mat. Sci., Vol. 6, pp. 1425-1432.

65. **Moriya, T. and Kawabata, A.** 1973, J. Phys. Soc. Jpn, Vol. 34, p. 639.

66. **Aharoni, A.** 12, 1984, J. Appl. Phys. , Vol. 56.

67. **see ref. of Aharoni, A. (1984).**

68. **Shimizu, M.** 1964, Proc. Phys. Soc. London, Vol. 84, p. 397.

69. **Mydosh, J.A.** *Spin Glasses: An Experimental Introduction.* London : Taylor & Francis, 1993.

70. **Muellner, N.C. and Kouvel, J.C.** 1972, Proc. Conf. Magn. and Magn. Materials, Vol. 5, pp. 487-491.

71. **Ubaid-Kassis, S. and Schroeder, A.** 5-9, 2008, Physica B: Condensed Matter, Vol. 403, pp. 1325-1327.

72. **Castro Neto, A.H., Castilla, G., and Jones, B.A.** 1998, Phys. Rev. Lett., Vol. 81, p. 3531.

73. **Vojta, T. and Hoyos, J.** 2008, Physica B, Vol. 403, pp. 1239-1241.

74. **Sampathkumaran, E.V. et al.** 2007, Phys. Rev. B, Vol. 75, p. 052412.

75. **Friedel, J.** 1958, Nuovo Cimento, Vol. 7, pp. 287 - 311.

76. **Collins, M.F. and Low, G.G.** 1965, Proc. Phys. Soc., Vol. 86, pp. 535 - 548.

77. **Lonzarich, G.G. and Taillefer, L.** 1985, J. Phys. C, Vol. 18, p. 4339.

78. **Skomshi, R.** *Simple Models of Magnetism.* New York : Oxford University Press, 2008.

79. **Case, M. and Dobrosavljevic, V.** 2007, Phys. Rev. Lett., Vol. 99, p. 147204.

80. **Vojta, T.** 2003, Phys. Rev. Lett., Vol. 90, p. 107202.

81. **Koorevaar, P. et al.** 1-2, 1995, Physica C: Superconductivity, Vol. 248, pp. 61-70.

82. http://web.mst.edu/~vojtat/research/research.html. [Online]